



# Reservoir simulation of fractured media in compressible single-phase flow in 2D, 2.5D and 3D unstructured gridding

Ali Zidane<sup>a</sup>, Abbas Firoozabadi<sup>a,b,\*</sup>

<sup>a</sup> Reservoir Engineering Research Institute, Palo Alto, CA, USA

<sup>b</sup> Yale University, New Haven, USA



## ARTICLE INFO

### Keywords:

Compressible flow  
Fractured media  
Mixed finite element  
Discontinuous Galerkin  
Cross flow equilibrium  
Discrete fractures  
IMPEC method  
Unstructured mesh  
Anisotropy  
Heterogeneous media

## ABSTRACT

This work presents an efficient and accurate algorithm for multicomponent compressible single-phase flow in fractured media. The model covers 2D, 2.5D and 3D unstructured gridding and accounts for heterogeneity and anisotropy. The fracture cross-flow equilibrium approach (FCFE) is applied in triangular finite elements (FE) in 2D and prism and tetrahedra (FE) in 2.5D and 3D, respectively. One can then simulate flow in fractured media with fractures in different orientations. Unstructured gridding with FCFE allows simulating realistic fractured porous media efficiently. In addition, FCFE in unstructured gridding alleviates the limitation of the number of intersecting fractures. In rectangular and hexahedron FE, the number is limited to 2 in 2D and 3 in 3D. To generate domains with complicated boundaries, we have developed a computer-aided design (CAD) interface. We demonstrate the efficiency and accuracy of our model by several numerical examples. Our examples include comparison with analytical solution and convergence rate.

## 1. Introduction

Modelling of compressible flow is of high interest in geochemical and petroleum subsurface formations. A challenge in subsurface simulation relates to flow in the fractures. Fractured porous media impose large range in spatial scales, permeabilities and fluxes, and generally have complex geometries. Using structured grids may not accurately describe the complexity. Commercial simulators may not converge in the near-well region because structured grids are not well suited to model radial flow near wells (Fung et al., 2013).

Numerous approximations are used for flow modelling in fractured media. These approximations are applied in single phase flow (Sandve et al., 2012; Ahmed et al., 2015; Hoteit and Firoozabadi, 2005) and multi-phase flow (Bastian et al., 2000; Granet et al., 1998; Bogdanov et al., 2003; Geiger et al., 2004, 2009; Abushaikhaa et al., 2015; Chen et al., 2015; Nick and Matthäi, 2011; Matthäi et al., 2007a,b; Unsal et al., 2010). The approximations are divided into two broad categories: the dual-continuum model and the discrete fracture-matrix model. The low computational cost of the dual-continuum models makes them attractive in modeling fracture networks (Warren and Root, 1963; Gilman and Kazemi, 1983). The dual-porosity model has been extended to multi rate transfer function (Di Donato et al., 2004; Geiger et al., 2013). The discrete fracture-matrix (DFM) model is known for high accuracy and

flexibility in fracture representation (Karimi-Fard et al., 2004; Kim and Deo, 2000; Reichenberger et al., 2006; Makedonska et al., 2015; Hyman et al., 2015; Hoteit and Firoozabadi, 2008; Zidane and Firoozabadi, 2014, 2017). The DFM approach geometrically matches the fracture and matrix grid-cells. When a lower dimension fractures representation is used, the fracture elements in DFM coincide with the matrix element interfaces. In addition to the classical DFM, Li and Lee (2008) proposed the embedded discrete fracture model (EDFM), it was later adopted by Moinfar et al. (2014). The EDFM is considered as a non-conforming DFM model. As a result, in EDFM, one could have more than four intersecting fractures even when applied on structured grids. The EDFM is known to have limitations to model low permeability fractures. Tene et al., (2017) presented the projection based EDFM (pEDFM) to overcome the limitations of the EDFM.

In this work we have selected the DFM for its attractive features in large scale and sparse fracture systems. We assume that the fracture aperture is small compared to the matrix scale (Noorishad and Mehran, 1982; Granet et al., 1998; Martin et al., 2005); therefore, the fractures are represented by  $(n-1)$ -dimensional elements in an  $n$ -dimensional domain.

The ease of implementation makes the finite difference (FD), and the finite volume (FV) approaches the most commonly used numerical methods in structured and unstructured grids, respectively. The FD and FV approaches are usually accompanied with a two-point flux approxi-

\* Corresponding author at: Yale University, New Haven, USA.

E-mail address: [abbas.firoozabadi@yale.edu](mailto:abbas.firoozabadi@yale.edu) (A. Firoozabadi).

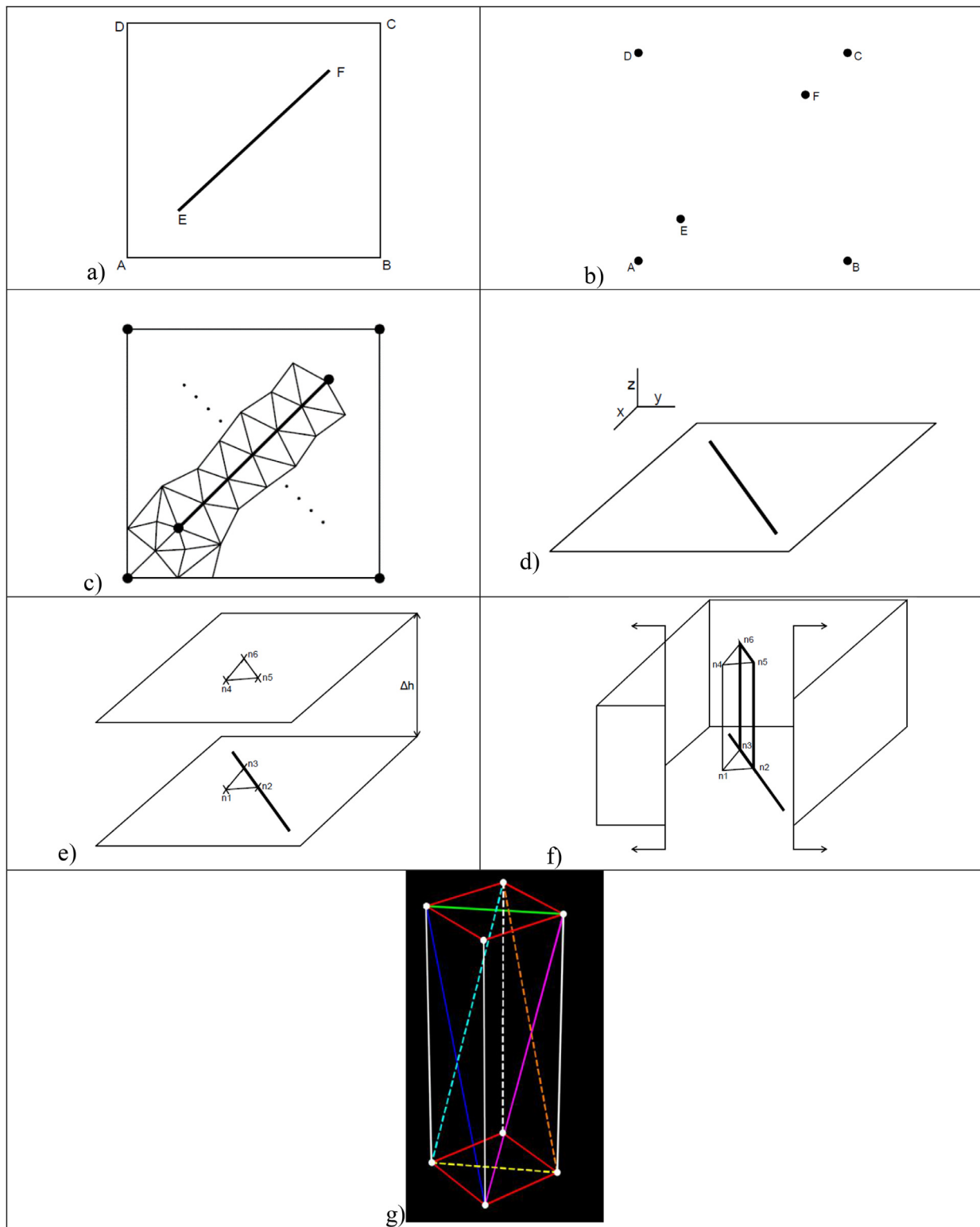


Fig. 1. 2D and 3D grid generation, thick lines represent the fractures.

mation (TPFA) to calculate the field fluxes. The FV method (Aavatsmark et al., 1998; Edwards, 2002; Edwards and Zheng, 2010; Lamine and Edwards, 2010, 2013) is more convenient to model oblique fractures (Karimi-Fard et al., 2004; Schmid et al., 2013). However, the coupling between the lowest-order methods and TPFA produces excessive numerical dispersion and suffers from grid sensitivity. To overcome the limitations of TPFA, the multipoint flux approximation (MPFA) has been in-

troduced (Aavatsmark, 2002; Kozdon et al., 2011; Huggenberger et al., 2015; Bastista et al., 2013; Nordbotten et al., 2007; Aavatsmark et al., 2008; Younes et al., 2013; Younes et al., 2015; Aavatsmark et al., 2010; Matringe et al., 2009; Salama et al., 2013; Wheeler and Yotov, 2006; Wheeler et al., 2011, 2012). The fluxes in MPFA are constructed from pressures in the surrounding elements making MPFA attractive in unstructured grids. However, MPFA may produce unphysical oscillations

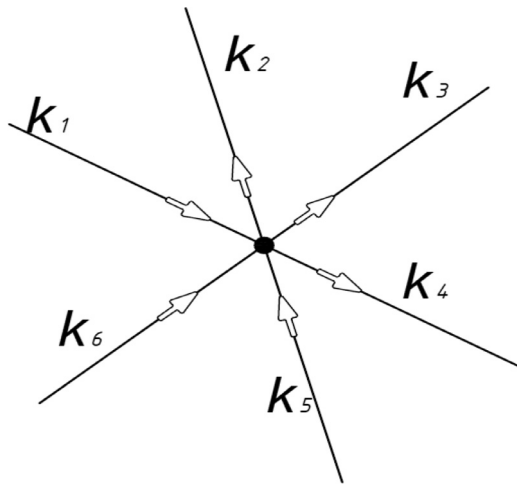


Fig. 2. Multiple intersecting fractures.

**Table 1**  
Relevant properties and initial conditions: Example 3.

Injection gas [mole%]	100 C <sub>1</sub>
Initial fluid in the domain [mole%]	100 C <sub>3</sub>
Pressure [bar]	50
Temperature [K]	397
Porosity [-]	0.2
Matrix permeability [md]	1
Fracture permeability [md]	1.d5
Fracture thickness [mm]	2
Injection rate [PV/year]	1.0

**Table 2**  
CPU time (min) with different number of fracture elements: Example 3.

Scenario	Fracture elements	CPU time (min)
Example 3-0	0	1.54
Example 3-1	10	1.61
Example 3-2	20	1.68
Example 3-3	30	1.78
Example 3-4	40	1.92
Example 3-5	50	1.96
Example 3-6	60	2.13
Example 3-7	70	2.21
Example 3-8	80	2.42

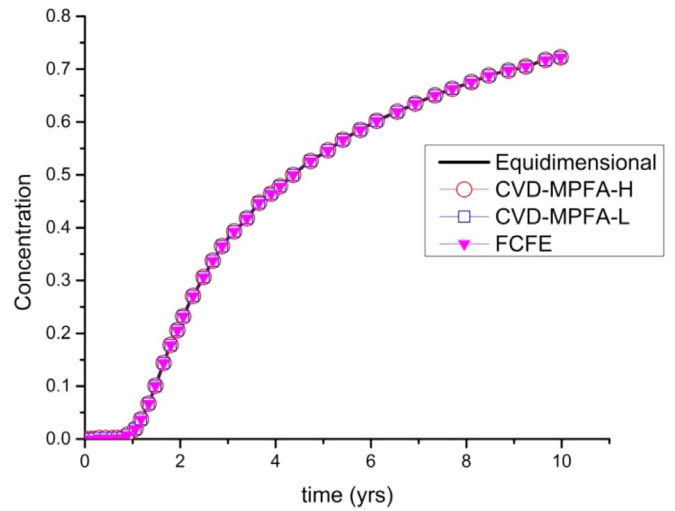


Fig. 4. Concentration vs. time at the production well: Example 1.

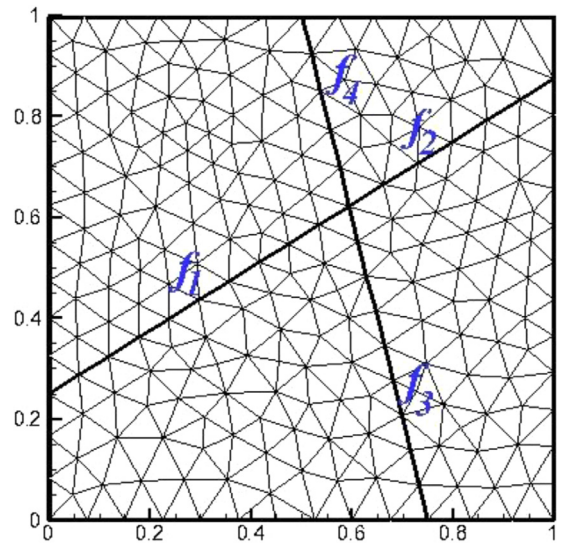


Fig. 5. Domain with fractures: Example 2.

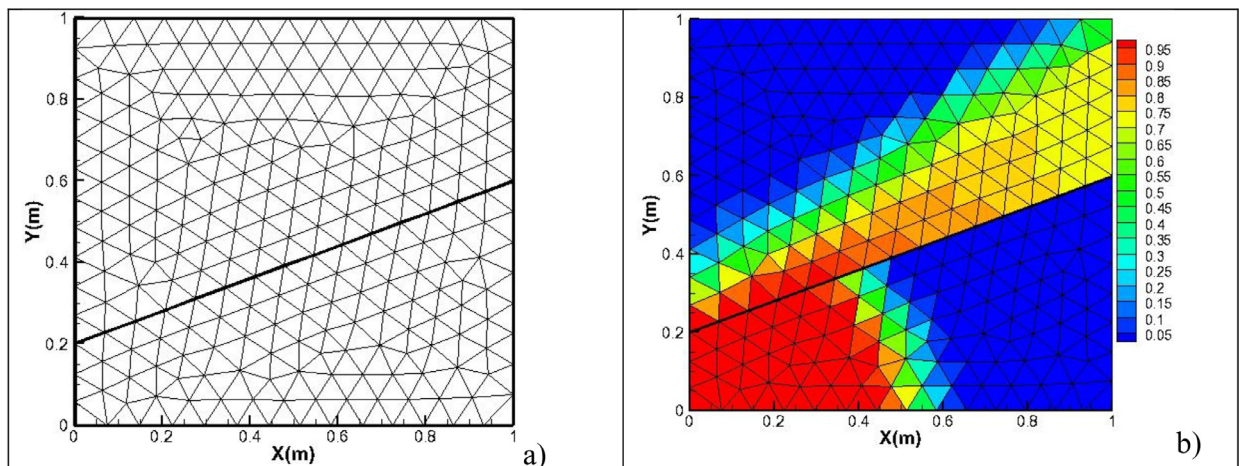


Fig. 3. Domain and mesh (a), and tracer concentration (b): Example 1.

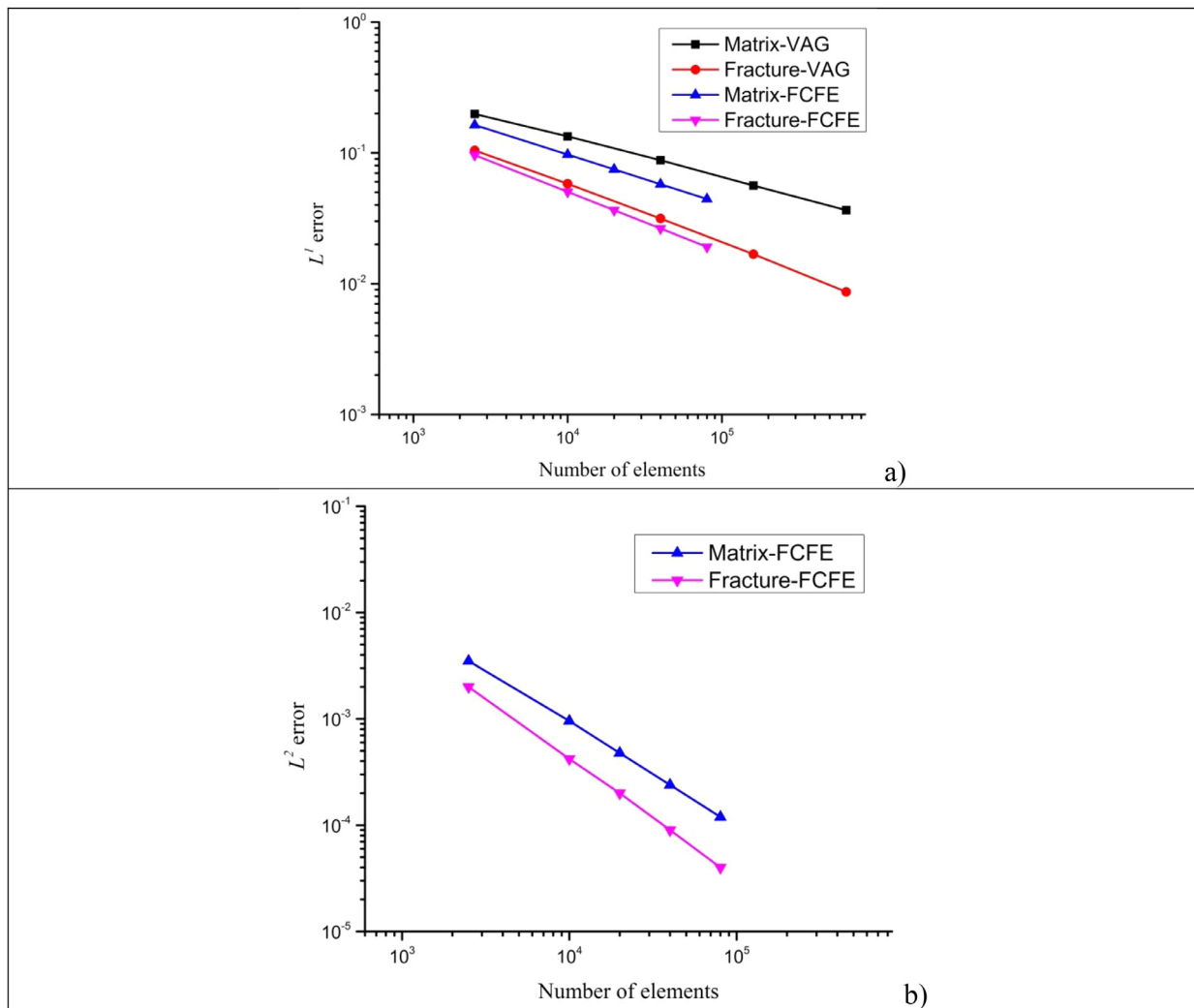


Fig. 6. Relative  $L^1$  (a) and  $L^2$  (b) errors: Example 2.

Table 3

Relevant properties and initial conditions: Example 5.

Injection gas [mole%]	100 CO <sub>2</sub>
Initial fluid in the domain [mole%]	100 C <sub>3</sub>
Pressure [bar]	50
Temperature [K]	397
Porosity [-]	0.2
Matrix permeability [md]	1
Fracture permeability [md]	1.45
Fracture thickness [mm]	1
Injection rate [PV/year]	1.0

in the pressure field (Nordbotten et al., 2007; Aavatsmark et al., 2008; Younes et al., 2014).

The use of finite element (FE) method in unstructured gridding has gained popularity since 1970s in many disciplines in science and engineering (Nejati et al., 2015; Moortgat and Firoozabadi, 2016). In this work we adopt the combination of the mixed finite element (MFE) method and the discontinuous Galerkin (DG) method. The MFE in its hybridized form provides pressure at the cell center and the traces of pressure at the cell interfaces. This ensures high accuracy in flux calculation in fractured reservoirs. The mass conservative DG method is used to discretize the mass transport equation. DG is particularly attractive in fractured reservoir simulation, because the approximation does not

have to be continuous between elements. By using DG in highly heterogeneous (fractured) media one can capture the discontinuity of concentration between the low permeable matrix and the high permeable fracture network.

The cross-flow equilibrium (CFE) concept in the discrete fracture approach was introduced to model multicomponent compressible flow in fractured porous media (Hoteit and Firoozabadi, 2005). In CFE, the pressure/concentration in a fracture element is assumed to be equal to the pressure/concentration in the surrounding matrix elements. This assumption requires the matrix grids next to fractures to be small. The small grid-cells may impose restriction on the size of time step due to the Courant–Freidricks–Levy (CFL) condition in explicit schemes. Later Hoteit and Firoozabadi (2008) advanced the efficiency of flow calculations in fractured media by the fracture cross-flow equilibrium (FCFE) approach in incompressible flow. In 2014, Zidane and Firoozabadi (2014) have used the FCFE to model multicomponent compressible flow in fractured porous media. In compositional extension it is assumed that both pressure and concentration are constant across the fracture width. Compared to CFE concept, the FCFE approach alleviates the need for small elements in the matrix grid cells. In our previous application the method was limited to structured grid-cells. In this work we apply for the first time the FCFE approach in compressible flow in 2D, 2.5D and in 3D for all commonly used finite elements (FE). Discretization of the pressure equation in compressible multicomponent flow is more complicated than the incompressible flow as we will show in the

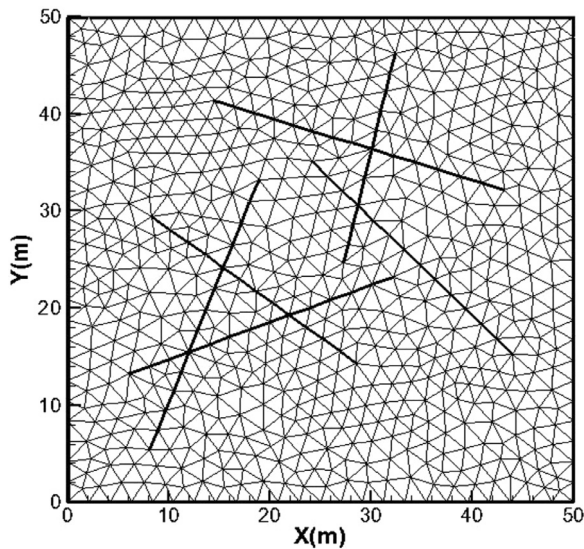


Fig. 7. Domain and fracture network: Example 3.

discretization section. Our model applies to quadrangular and triangular elements in 2D and to hexahedra, prism and tetrahedra elements in 3D. In addition, we have developed for the first time a computer-aided design (CAD) interface coupled with our mesh generator. This allows

the user to generate very complicated fractured domains in an efficient way.

Unstructured grids offer several advantages over structured grids in reservoir simulation. The advantages include the ease to simulate fractured reservoirs in which fractures have different orientations. A triangular finite element could be oriented in different directions such that one (or more) of its edges is (are) aligned with the fractures. One of the challenges is to generate unstructured triangular grids that some elements are aligned to the orientation of the different fractures. We highlight the two dominant methods in unstructured triangular grid generation and justify our choice for one of the two. In one, the advancing front method, the cells that make up the interior of the mesh are modeled by marching away from the boundaries of the domain (Anderson 1994). The other method is the Delaunay triangulation. The Delaunay technique triangulates a set of points in such a way that no extremely skewed cells are generated. In the Delaunay triangulation one can have the points on the desired edges to be part of the field points generated a priori when using the FCFE model. The details of the Delaunay triangulation are presented in Anderson (1994). In 2.5D one uses prism type FE extruded from 2D triangular elements as we will explain later. Prism FE provides a more realistic representation of the fractures compared to hexahedron FE in DFM. In 3D we use fully unstructured tetrahedron grids. Similarly to 2D, in 2.5D and 3D the fractures are also represented by the interfaces of the FE.

We provide a description of the proposed model in generating unstructured 2D and 3D grids in the next section. Then we present the differential equations that describe multicomponent compressible flow in fractured media and a brief overview on the discretization of the pres-

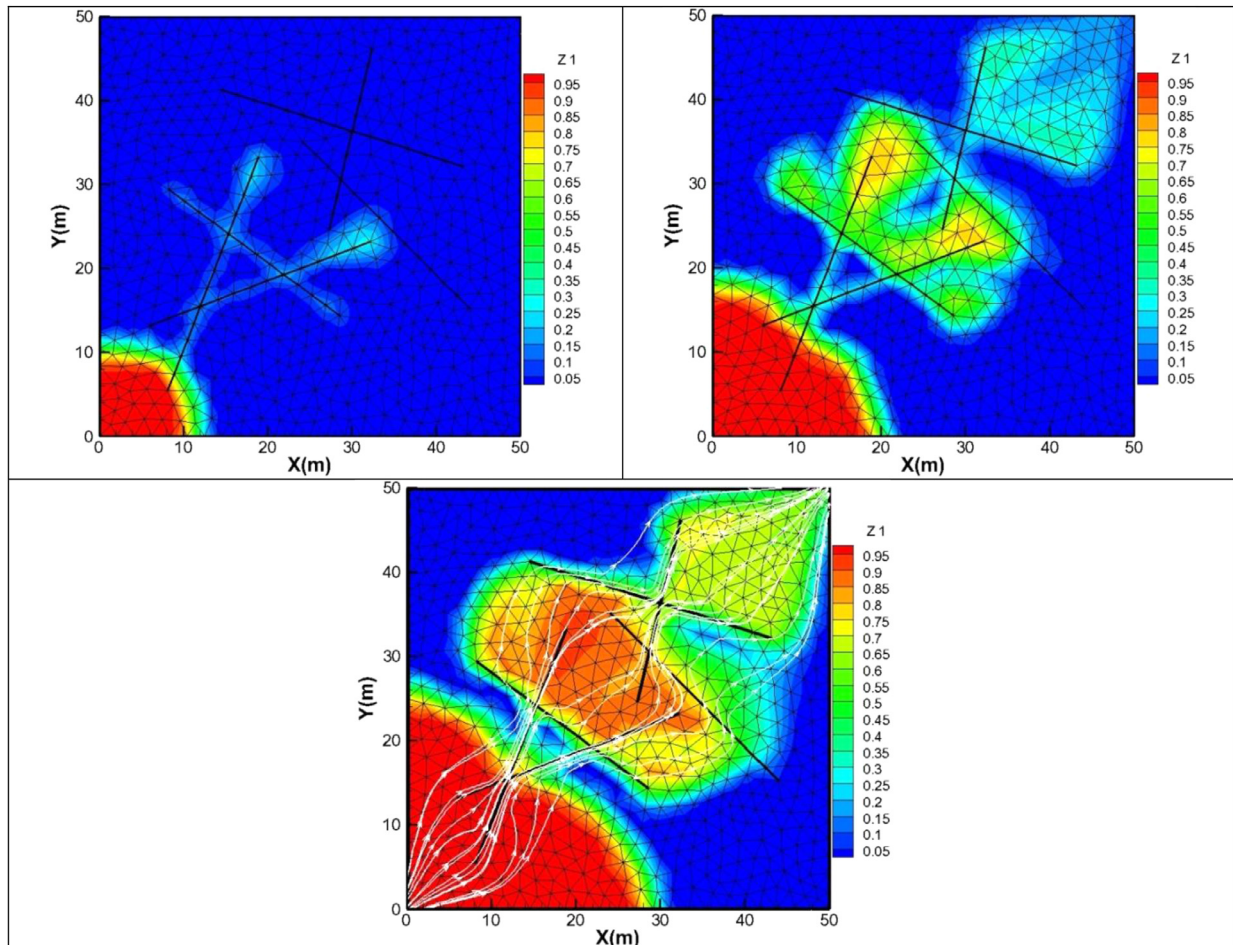


Fig. 8. Overall mole fraction of methane at 5% PVI (a), 25% PVI (b) and 70% (c) (white lines represent streamlines at 70% PVI): Example 3.

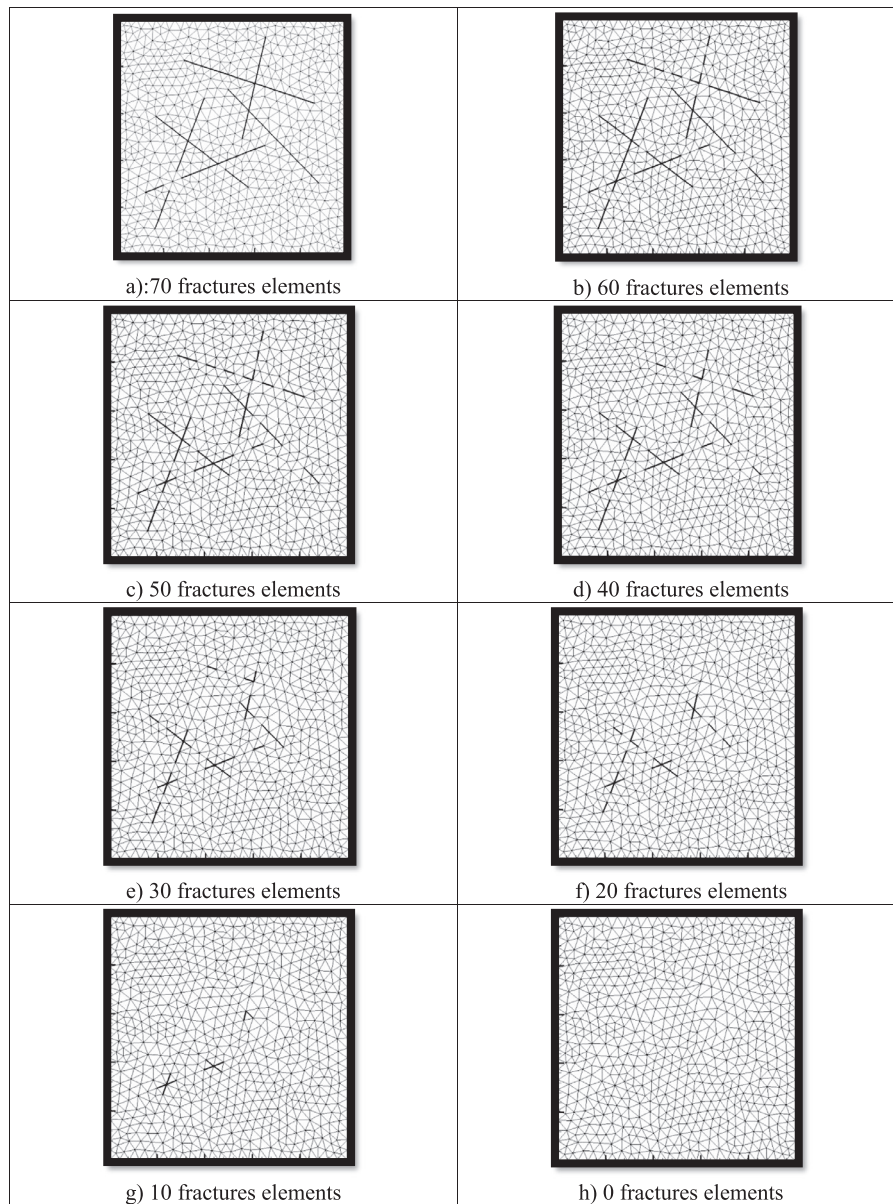


Fig. 9. Meshes with reduced fracture elements (domain size  $50 \times 50 \text{ m}^2$ ): Example 3.

sure and the species mass balance equations in the rock matrix and the fracture network. We provide several examples to highlight the features of the model and conclude with few remarks.

## 2. Model description

For completeness we briefly present the main features of our model which combines different spatial and temporal discretization schemes in the matrix and in the fracture network to advance efficiency and accuracy. The basis and test functions in the numerical discretization for different types of FEs are presented in [Appendix A](#). The essences of the model are:

- The hybridized mixed finite element method (MFE) is used to calculate the fluxes in the matrix domain and the fracture network ([Durlafsky, 1994](#); [Mosé et al., 1994](#); [Darlow et al., 1984](#); [Hoteit and Firoozabdi, 2008](#); [Younes et al., 2011](#); [Zidane et al., 2012](#); [Zidane et al., 2014a](#); [Zidane et al., 2014b](#); [Zidane and Firoozabadi, 2014](#); [Zidane and Firoozabdi, 2015](#)). The MFE formulation can readily accommodate full permeability tensors.
- The discontinuous Galerkin (DG) method is used to solve the mass balance equations in the matrix. A slope limiter is used to remove the nonphysical oscillations ([Cockburn and Shu, 1989, 1998](#); [Younes et al., 2014, 2015](#); [Chavent and Jaffré 1986](#); [Hoteit et al., 2004](#); [Siegel et al., 1997](#)).
- A finite volume approach is used to discretize the species mass balance equations in the fractures.
- The traces of the pressure in the matrix and the fracture network are implicitly updated at each time step.
- The molar densities in the fracture network are implicitly updated at each time step.
- The molar densities in the matrix domain are explicitly updated at each time step. The implicit pressure-explicit concentration (IMPEC) approach in the matrix domain is found to be stable and efficient in single-phase flow and also in multiphase compositional flow as demonstrated in [Moortgat and Firoozabadi \(2016\)](#) and [Zidane and Firoozabdi \(2017\)](#). However, an IMPEC approach is not efficient when used in the fractures. This is due to the small size of the fracture elements that impose a severe restriction on the size of time

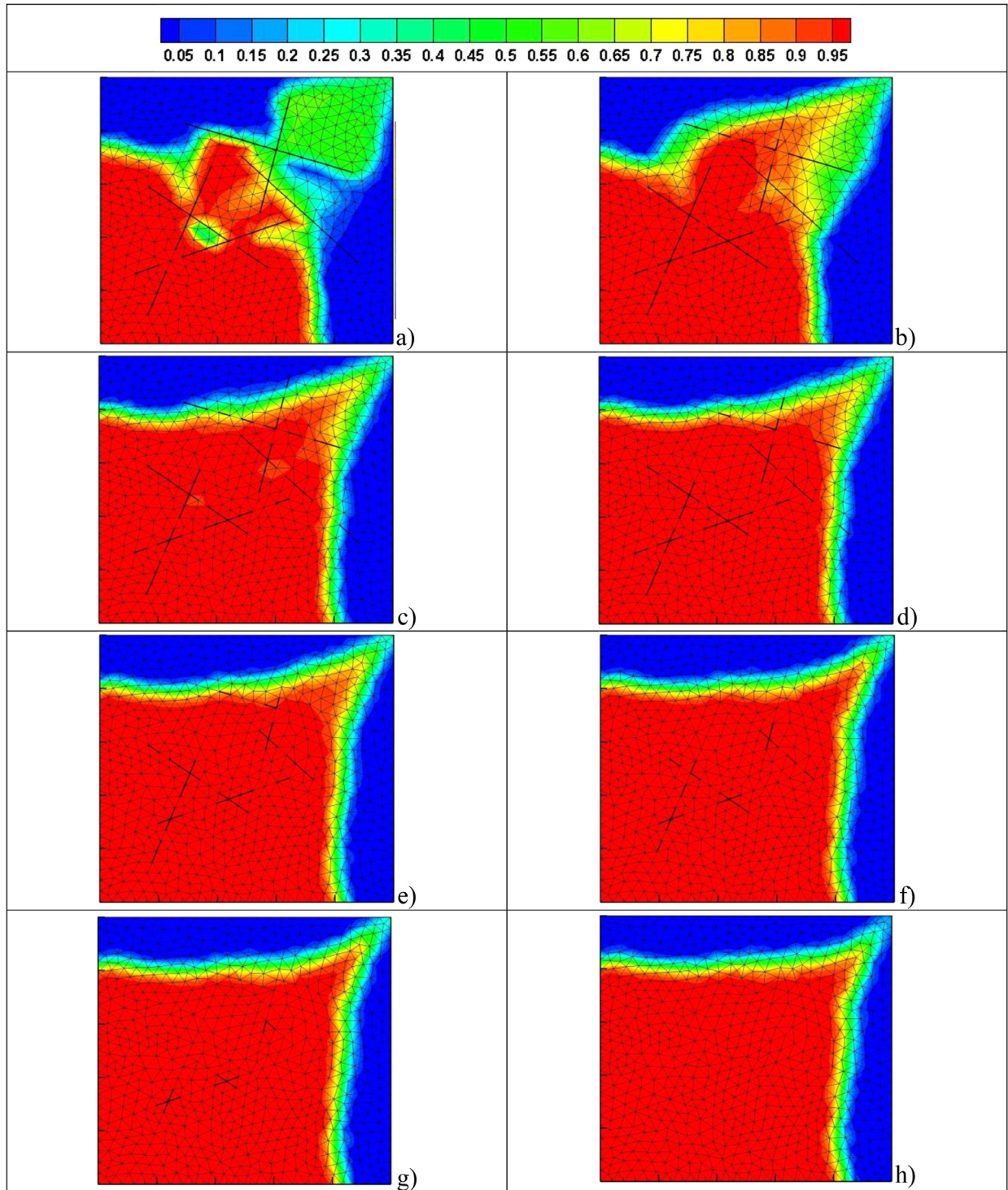


Fig. 10. Overall mole fraction of methane at 70% PVI in domains with reduced fracture elements (domain size  $50 \times 50 \text{ m}^2$ ): Example 3.

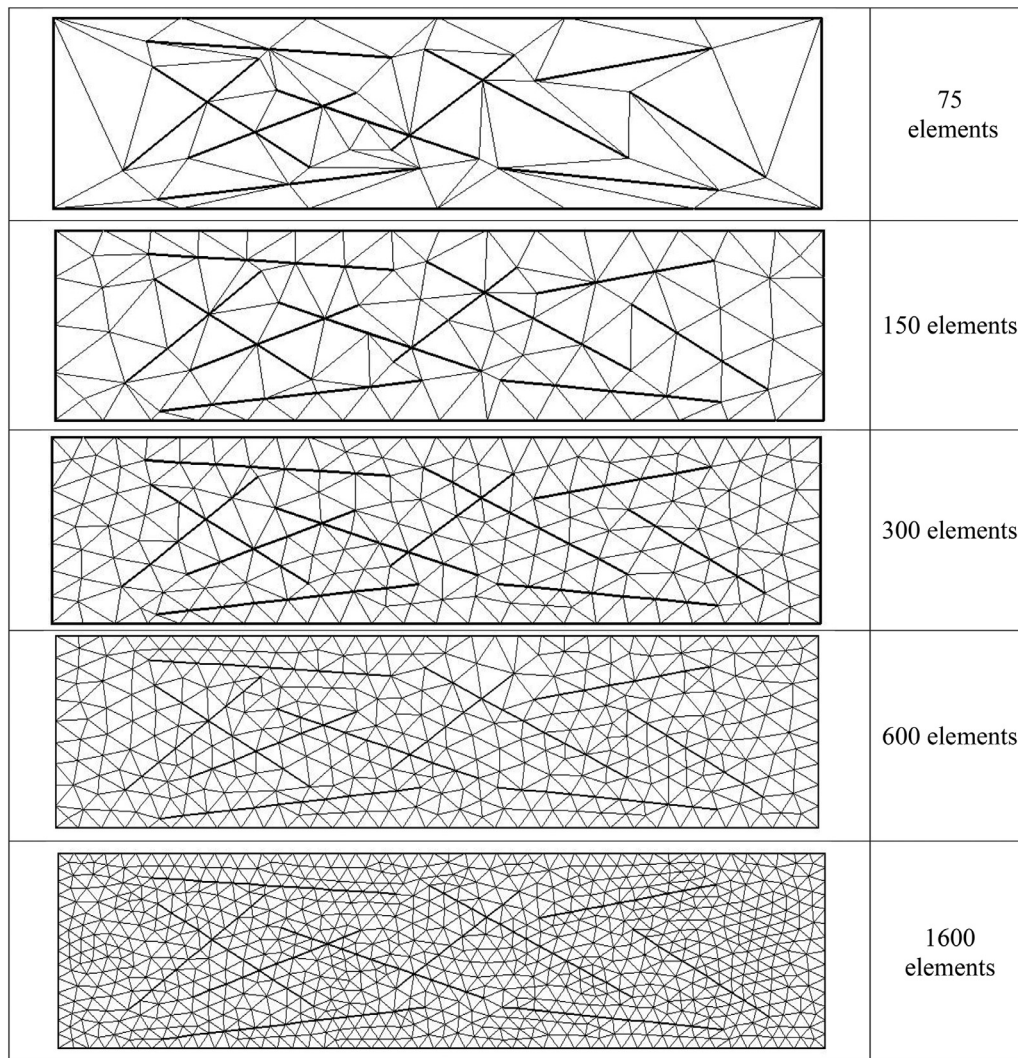


Fig. 11. Domain and meshes; fractures are represented by thick black lines (domain size  $1000 \times 300 \text{ m}^2$ ): Example 4.

step. Therefore we adopt an implicit time scheme in the fracture network. The larger size of the matrix elements justifies the use of an explicit discretization in the matrix domain instead of a fully implicit scheme.

- Unstructured triangular elements are used in 2D, and prism and tetrahedron elements are used in 3D.

### 3. Unstructured 2D, 2.5D and 3D grid generation

Triangular elements allow simulating oblique fractures (Fig. 1a) without imposing approximations on the matrix elements (Reiter et al., 2012). In FCFE, the set of points that define the domain and the locations of the fractures should be provided a priori (Fig. 1a, b). The grids are then generated by starting from the domain and the fracture input data points (Fig. 1c). In rectangular domains and a small number of fractures (Fig. 1b) the set of points could be manually generated. However, this technique is not efficient when the domain boundaries are complex and the number of fractures is high. To overcome this deficiency we have developed an interface to read data points from a CAD (Computer-aided design) output. CAD software is usually used to create two and three dimensional graphical representations of physical objects. Using a CAD

Table 4

Relevant properties and initial conditions: Example 7.

Pressure [bar]	115
Temperature [K]	397
Porosity (zone1) [-]	0.1
Porosity (zone2) [-]	0.2
Matrix permeability [md] (zone1)	0.1
Matrix permeability [md] (zone2)	10
Fracture permeability [md]	1. d5
Fracture thickness [mm]	1
Injection rate [PV/year]	0.1

interface makes it possible to generate very complex boundaries (as will be shown in the examples) rapidly. In addition, the CAD software allows reading pre-existing maps/domains that have “dwg, dws, dwt and dxf” extensions and edit them by adding/removing boundary and/or fracture points. Unstructured prism FE is used in 2.5D. The prisms are constructed from triangular 2D surfaces (Fig. 1d). The 2D triangles are then extruded to as many layers as required (Fig. 1e) and extrude the edges of the triangles to 2D planes in space. The technique can generate



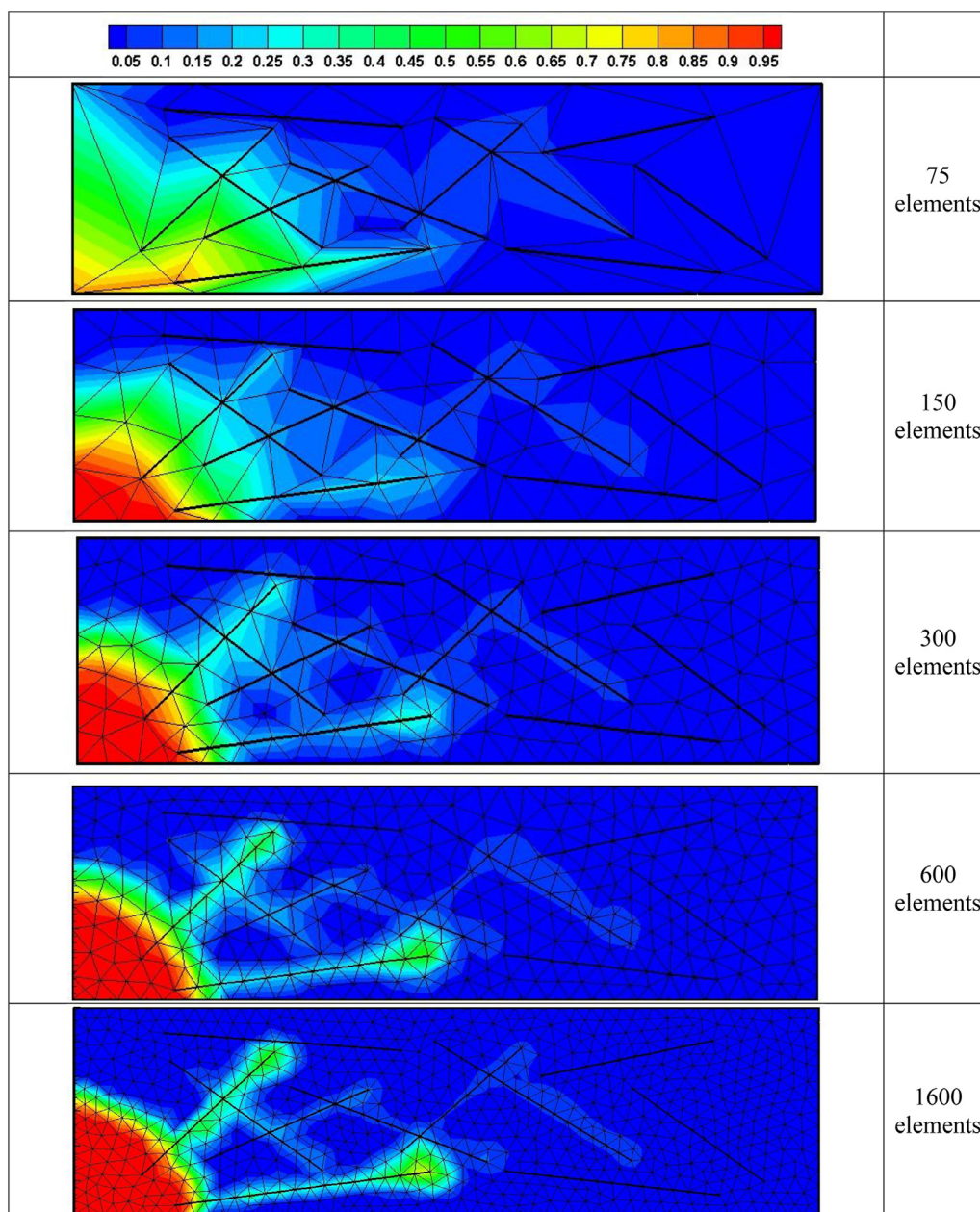


Fig. 12. Overall mole fraction of methane at 10% PVI with the different meshes (domain size  $1000 \times 300 \text{ m}^2$ ): Example 4.

**Table 5**  
Compositions of initial and injected fluids: Example 7.

Component	Initial [mole %]	Injected [mole %]
CO <sub>2</sub>	0.00	100
C <sub>1</sub>	5	0
C <sub>2</sub>	6	0
C <sub>3</sub>	15	0
C <sub>4</sub>	9	0
C <sub>5</sub>	22	0
C <sub>6</sub>	19	0
C <sub>7</sub>	24	0

several layers of a reservoir and assign different properties to each layer as will be demonstrated later in the examples. The edge defining the

fracture in 2D by two nodes (e.g.  $n_2$ - $n_3$  Fig. 1e); the extruded nodes of this edge ( $n_5$ - $n_6$  Fig. 1f) are defined as fracture nodes in 3D. The pre-existing nodes and the extruded nodes define a fracture element in 3D (Fig. 1f). Tetrahedra are used in full 3D discretization and they are generated by dividing a hexahedra FE into 6 tetrahedra and by using Tetgen (see Fig. 1g) (Si 2011).

#### 4. Mathematical model

##### 4.1. Governing equations in the matrix

The rock matrix and the discrete fractures in our model have different geometrical dimensions in the simulation domain ( $n$ -D for the matrix domain and  $(n-1)$ -D for the fracture network). The governing equations

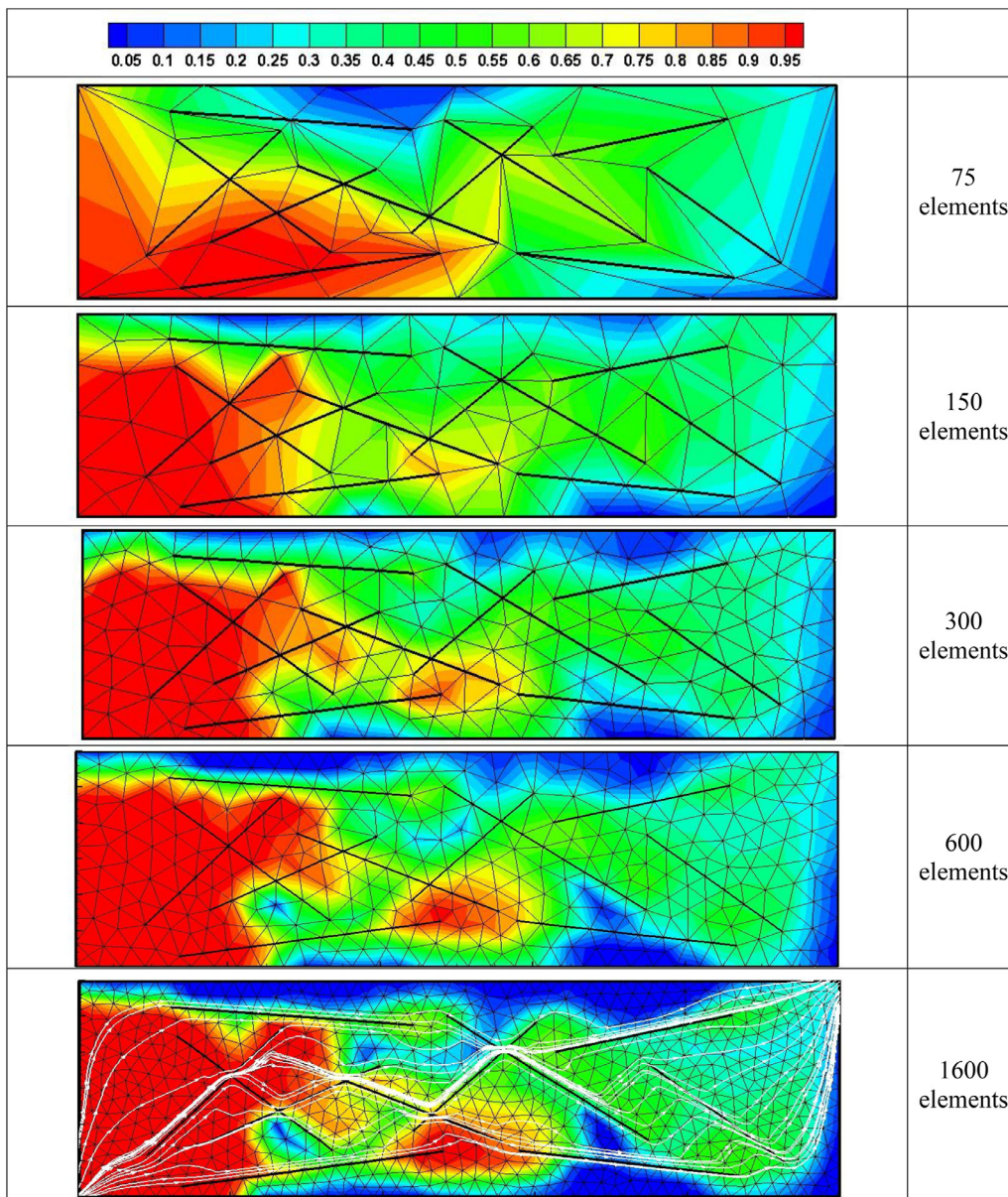


Fig. 13. Overall mole fraction of methane at 60% PVI with the different meshes (white lines in the 1600 elements plot represent the streamlines; domain size  $1000 \times 300 \text{ m}^2$ ): Example 4.

are, therefore, treated separately. The superscript  $m$  denotes the matrix; the superscript  $f$  denotes the fractures. The mass balance of component  $i$  in miscible and compressible flow is given by the following equation:

$$\phi^m \frac{\partial c_i^m}{\partial t} + \nabla \cdot (c_i^m v^m) - f_i^m = 0, \quad i = 1 \dots n_c \quad \text{in } \Omega \times (0, \tau) \quad (1)$$

In the above equation,  $\phi$  denotes the porosity,  $v$  the velocity field,  $c_i = cz_i$  the molar density of component  $i$  where  $c$  is the overall molar density;  $z_i$  and  $f_i$  are the mole fraction and the sink/source term of component  $i$  in the mixture, respectively.  $\Omega$  is the computational domain and  $\tau$  denotes the simulation time and  $n_c$  is the number of components.

The flow in porous media is described by Darcy's law:

$$v = -\frac{k}{\mu} (\nabla p - \rho g) \quad (2)$$

where  $k$  is the absolute permeability tensor,  $\mu$  the dynamic viscosity,  $p$  the pressure,  $\rho$  the mass density and  $g$  the gravitational acceleration.

The Peng–Robinson equation of state (EOS) (Peng and Robinson, 1976) is used to describe the molar density  $c$  as a function of the composition, temperature and pressure as follows:

$$c = \frac{p}{ZRT}$$

$$Z^3 - (1 - B)Z^2 + (A - 3B^2 - 2B)Z - (AB - B^2 - B^3) = 0 \quad (3)$$

$Z$  is the compressibility factor,  $R$  the gas constant,  $T$  the temperature, and  $M_i$  the molar mass of component  $i$ . To complete the system of equations, we use the volume balance approach from Acs et al. (1985) and Watts (1986) to compute the pressure field in compressible flow. The

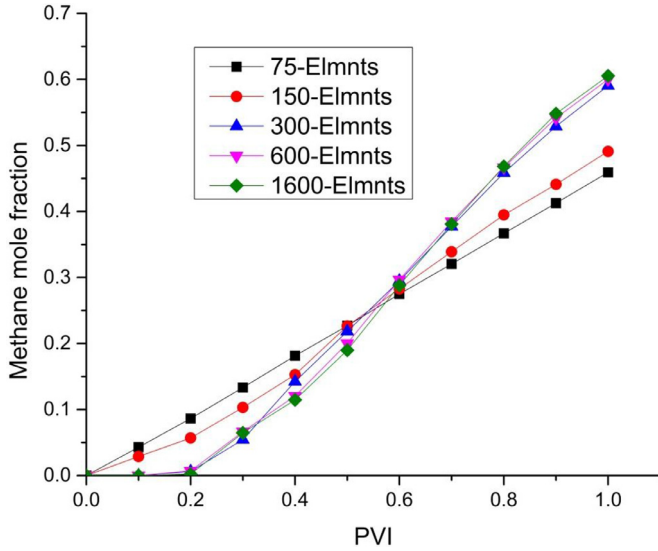


Fig. 14. Overall mole fraction of methane at the production well with different mesh refinements: Example 4.

expression for the volume balance is given by:

$$\theta^m C_i^m \frac{\partial p^m}{\partial t} + \sum_{i=1}^{n_c} \bar{V}_i^m (\nabla \cdot (c_i^m v^m) - f_i^m) = 0 \quad (4)$$

where  $C_i$  is the total compressibility,  $\bar{V}_i$  is the total partial molar volume of component  $i$  in the mixture (Firoozabadi 2015).

#### 4.2. Governing equations in the fractures

The mass balance equations in the fractures integrated along the fracture width  $\epsilon$  in  $(n-1)$ -D are expressed by:

$$\theta^f \frac{\partial c_i^f}{\partial t} + \nabla \cdot (c_i^f v^f) - \bar{Q}_i^f - f_i^f = 0, \quad i = 1 \dots n_c \quad (5)$$

The term  $\bar{Q}_i^f$  is the mass flux of component  $i$  across the matrix-fracture boundaries in the mixture.

Similarly to the matrix domain, the pressure field in the fractures is obtained from:

$$\theta^f C_i^f \frac{\partial p^f}{\partial t} + \sum_{i=1}^{n_c} \bar{V}_i^f (\nabla \cdot (c_i^f v^f) - \bar{Q}_i^f - f_i^f) = 0 \quad (6)$$

### 5. Numerical discretization

#### 5.1. Discretization of the flow equation

The hybridized mixed finite element (MFE) method with the lowest order Raviart–Thomas (RT) basis space is used to discretize the volumetric flow in the matrix and the fractures. The global system of equations for the pressure is obtained by writing the continuity of fluxes and pressures at all the interfaces of the matrix elements and the fractures elements. The number of unknowns equals the number of interfaces in the matrix domain ( $Tp^m + p^f$ ) plus the number of interfaces in the fracture network ( $Tp^f$ ).

$$\begin{bmatrix} A^{m,m} & A^{m,f} & 0 \\ A^{m,f} & A^{f,f} & -\bar{R}^f \\ 0 & R^{T,f} & M^f \end{bmatrix} \begin{bmatrix} Tp^m \\ P^f \\ Tp^f \end{bmatrix} = \begin{bmatrix} V^m \\ V^f \\ 0 \end{bmatrix} \quad (7)$$

Derivation of Eq. (7) and the definition of all elements are given in Appendix A.

#### 5.2. Discretization of the transport equations

The DG method is used to discretize the species transport equations in the matrix with an explicit time scheme. Multiplying the first expression in Eq. (1) by the shape function  $\varphi_{K,l}$  and integrating over each matrix element  $K$  we get:

$$\sum_{i=1}^{n_j} \frac{d c_{i,K,j}^m}{dt} \int_K \theta_K^m \varphi_{K,l} \varphi_{K,j} = \int_K \varphi_{K,l} f_i^m + \sum_{j=1}^{n_j} \sum_{E=1}^{n_E} q_{K,E} \left( c_{i,K,j}^m \int_K \varphi_{K,j} w_{K,E} \nabla \varphi_{K,l} - \frac{\bar{c}_{i,K,E,j}^m}{|E|} \int_E \varphi_{K,l} \varphi_{K,j} \right) \quad (8)$$

In the above equation for a matrix element  $K$ ,  $c_{i,K,j}^m$  is the molar density of component  $i$  at node  $j$ ,  $n_j$  is the number of nodes,  $\bar{c}_{i,K,E,j}^m$  is the upstream molar density of component  $i$  at node  $j$  of interface  $E$ ,  $q_{K,E}$  is the volume flux across the interface  $E$  and  $n_E$  is the total number of interfaces in matrix element  $K$ .

The system of ordinary differential equations of order  $n_j$  (per element) is obtained by writing Eq. (8) over each element  $K$  in the matrix domain coupled with a slope limiter stabilization to remove the non-physical oscillations.

As opposed to the matrix elements, the mass balance equation in the small fracture elements is discretized with an implicit time scheme to overcome the CFL restriction. To avoid the expensive DG approximation in the fractures, a finite volume method is applied in the fractures as follows:

$$\theta_k^f \frac{c_{i,k}^{f,n+1} - c_{i,k}^{f,n}}{\Delta t} + \sum_{e=1}^{n_e} \bar{c}_{i,e}^{f,n} q_{k,e}^{f,n} = \bar{Q}_i^{f,K_1} + \bar{Q}_i^{f,K_2} + f_{i,k}^{f,n} \quad (9)$$

where  $\bar{c}_{i,e}^{f,n}$  denotes the upstream value of the molar density. The term  $\bar{Q}_i^{f,K_j}$  ( $j = 1, 2$ ) represents the matrix/fracture exchange flux. The discretization in the fractures and coupling the fracture network with the matrix domain are presented in Appendix B. The above equation is written for all the fracture elements and the system of equations are linearized and solved using the Newton–Raphson (NR) method.

#### 5.3. Upstream technique for multiple intersecting fractures

In structured grids, the maximum number of intersecting fracture elements at one interface is four. In unstructured grids the maximum number of intersecting fracture elements may be higher; in principle it depends on the mesh quality and the order of refinement near the fractures. In two intersecting fractures, the upstream value is deduced from the flux direction. When  $n_t$  fractures intersect at point  $O$ , and  $n_u$  is the number of fractures with fluxes in the upstream direction (Fig. 2), the upstream value at the intersection is given as follows (Zidane and Firoozabadi, 2014):

$$c_{i,O}^f = \frac{\sum_{j=1}^{n_u} c_{i,k_j}^f q_{k_j}^f}{\sum_{j=1}^{n_u} q_{k_j}^f} \quad (10)$$

### 6. Numerical examples

We present in the following seven examples with different number of fractures and different geometries. In addition to the examples, we present in Appendix C a pinch-out problem and a domain with oblique fracture in 3D in Appendix D. The implementation of a barrier in FCFE is demonstrated in Appendix E, and one example with anisotropy is studied in Appendix F. An Intel Core-i5 PC, 3 GHZ CPU, 4 GBRAM is used in all the runs. CPU time is for 1 pore volume injection (PVI) unless specified otherwise.

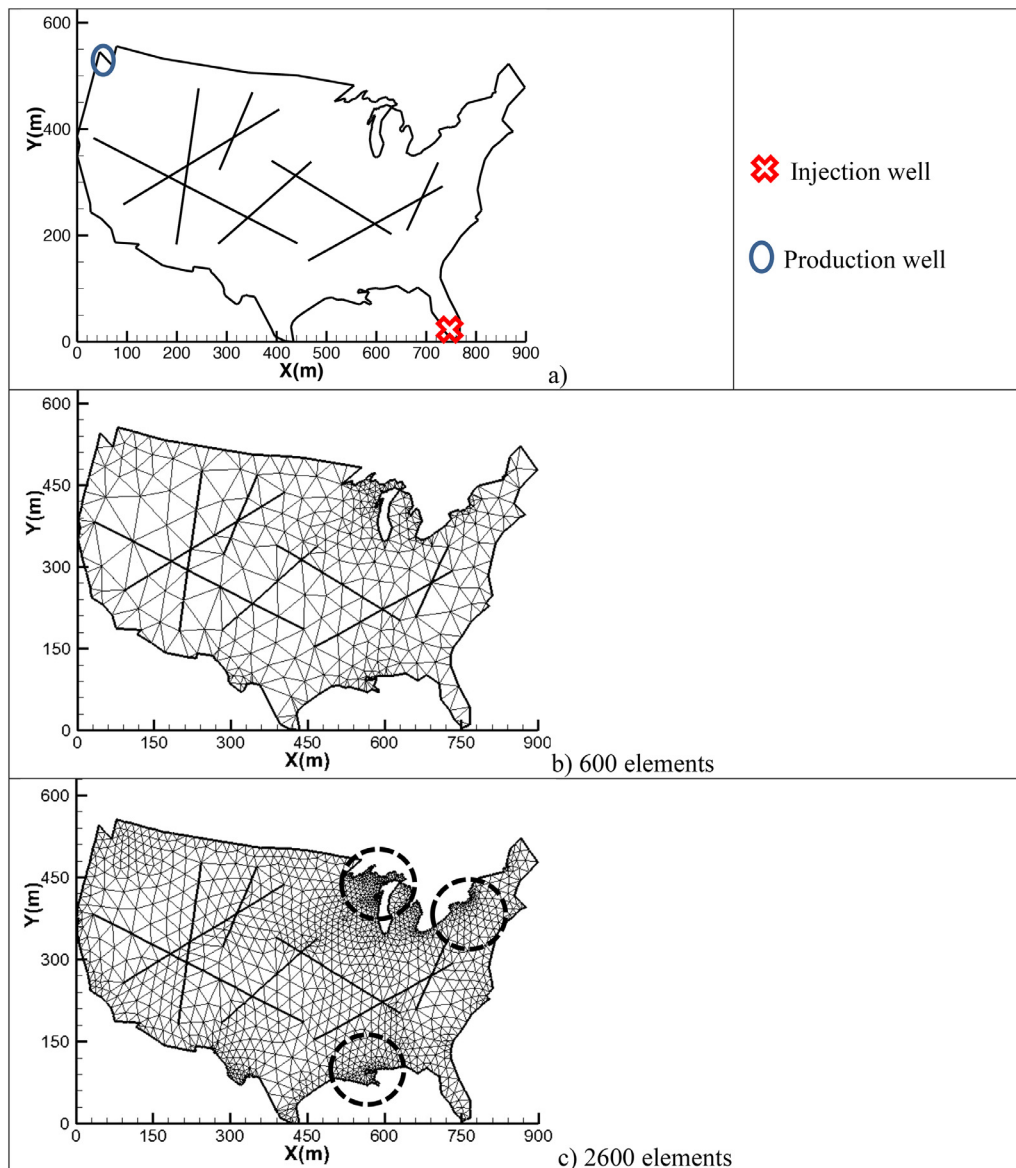


Fig. 15. Domain with locations of injection and production wells (a), and meshes (b and c) (thick black lines represent the fractures): Example 5.

### 6.1. Example 1: Single fracture

In this example we consider the single fracture problem from Ahmed et al. (2015). The domain is  $1\text{ m} \times 1\text{ m}$  with one oblique fracture (Fig. 3a). The fracture thickness is  $1\text{ mm}$  with  $10^4\text{ md}$  permeability. The permeability of the matrix is  $1\text{ md}$ . The injector is located at one corner and production at constant pressure is at the opposite corner. The injection rate is  $0.3171\text{ PV/year}$ . A Neumann boundary condition with zero flux is imposed on the domain boundary. We compare the results of our model to the control-volume distributed multipoint flux approximation model with lower dimensional fractures (or CVD-MPFA-L) (Ahmed et al., 2015) and the hybrid (Sandve et al., 2012) (CVD-MPFA-H) and to the equidimensional model where fractures are represented by the same dimension as the matrix elements. Note that Eq. (4) should be reduced to incompressible single-phase flow to make the problem the same as in Ahmed et al. (2015). The tracer concentration at the production well is recorded throughout the simulation and com-

pared to the results of the three different models. As shown in Fig. 4 an excellent agreement is observed between our model (FCFE) and CVD-MPFA-L, and CVD-MPFA-H and the equidimensional model. In Fig. 3b we show the tracer concentration at  $1.2\text{ PVI}$ . The contour profile is similar to the one by Ahmed et al. (2015) in the tracer incompressible flow.

### 6.2. Example 2: Intersecting fractures

We compare our model to the vertex approximate gradient (VAG) finite volume scheme and the results to an example presented in Xing et al. (2016). The importance of this example is the analytical solution provided by the authors (Xing et al., 2016). Comparing our numerical results to an exact solution demonstrates the accuracy of the model. The domain of unit surface area contains four intersecting fractures that we denote by  $f_1, f_2, f_3$  and  $f_4$  (Fig. 5). The fracture to matrix permeability ratio is  $200$  for  $f_1$  and  $f_2$ , and  $400$  for  $f_3$  and  $f_4$ . The fracture aperture

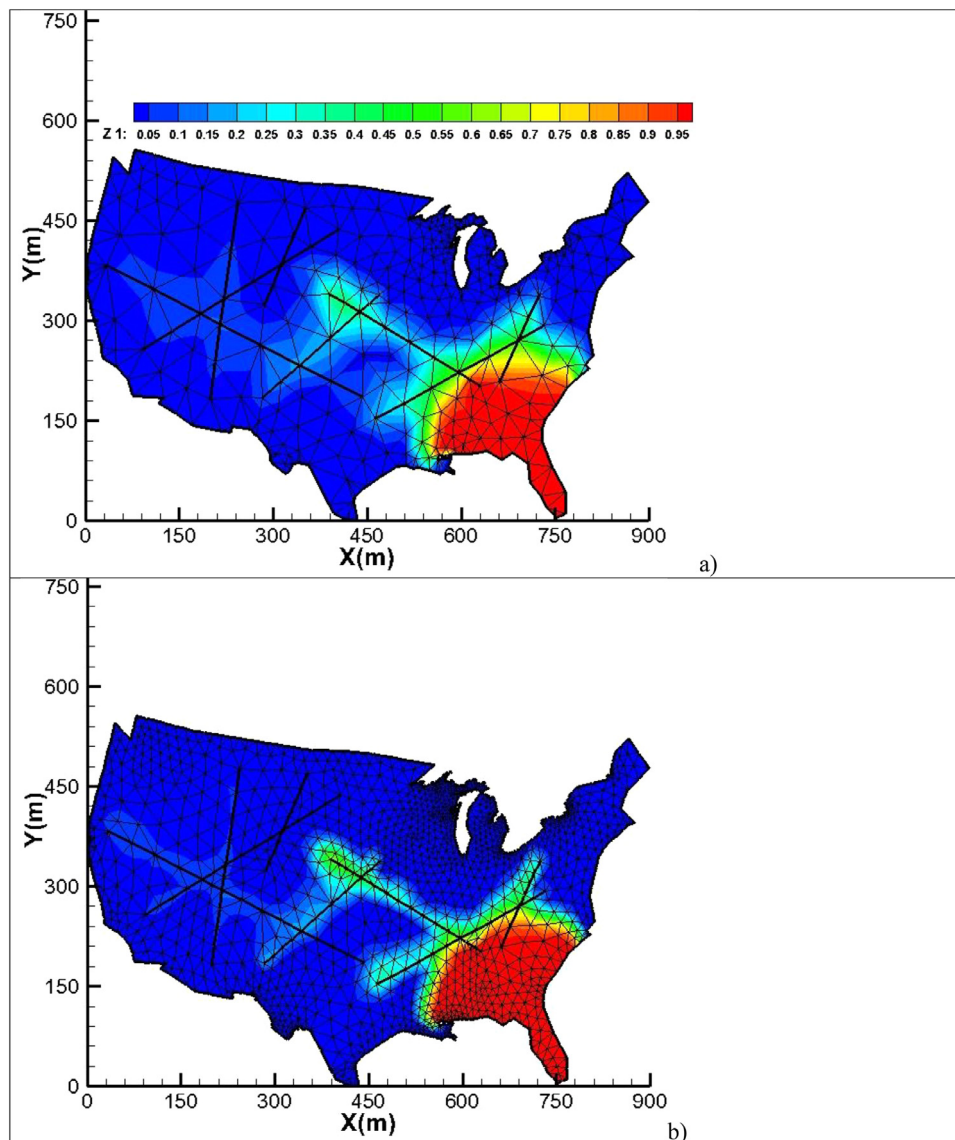


Fig. 16. Overall mole fraction of CO<sub>2</sub> at 10% PVI with 600 elements (a) and 2600 elements (b): Example 5.

is 0.01 for all fractures. Porosity is set to one in the whole domain. In Fig. 6 we show the convergence of the relative  $L^1$  and  $L^2$  errors between the analytical solution and the numerical solution of our model and the model of Xing et al. (2016) at different mesh refinements in the matrix and the fractures. As shown in Fig. 6 the error in our model is less than the VAG model in both the matrix and the fractures even with lower mesh refinement in our model. The error difference between our model and VAG is more significant in the matrix domain than the fractures. This is because of the accuracy of our higher-order DG results in the matrix.

### 6.3. Example 3: CPU time

In this example we consider a network of intersecting fractures as shown in Fig. 7. The properties of the domain are given in Table 1. Locations of injection and production wells are the same as in Example 1. The overall mole fraction of methane is shown in Fig. 8 at differ-

ent PVIs. The total number of matrix elements is 1400. The fracture network includes 80 (n-1)-D elements. Higher number of fracture elements implies a larger matrix to be inverted during the NR iterations (see Eq. (9)). To evaluate the effect of the number of fracture elements on the CPU time, we randomly remove 10 fracture elements from the fracture network. The order and/or location of the randomly removed fractures does not affect the CPU cost. As a result, the new domain has 70 (n-1)-D fracture elements. This procedure is repeated 8 times by reducing the number of fracture elements 10 at a time (see Fig. 9a to g). In the 8th reduction, the problem reduces to unfractured media (Fig. 9h). We show in Table 2 the CPU time at 100% PVI for different cases with different number of fractures from 0 (unfractured media) to 80 fracture elements (shown in Fig. 7). In Fig. 10 we show the overall mole fraction of methane at 70% PVI at different fracture reductions. The small increase in the CPU time from 1.54 min for unfractured media to 2.42 min (80 fracture elements) demonstrates the efficiency of our model.

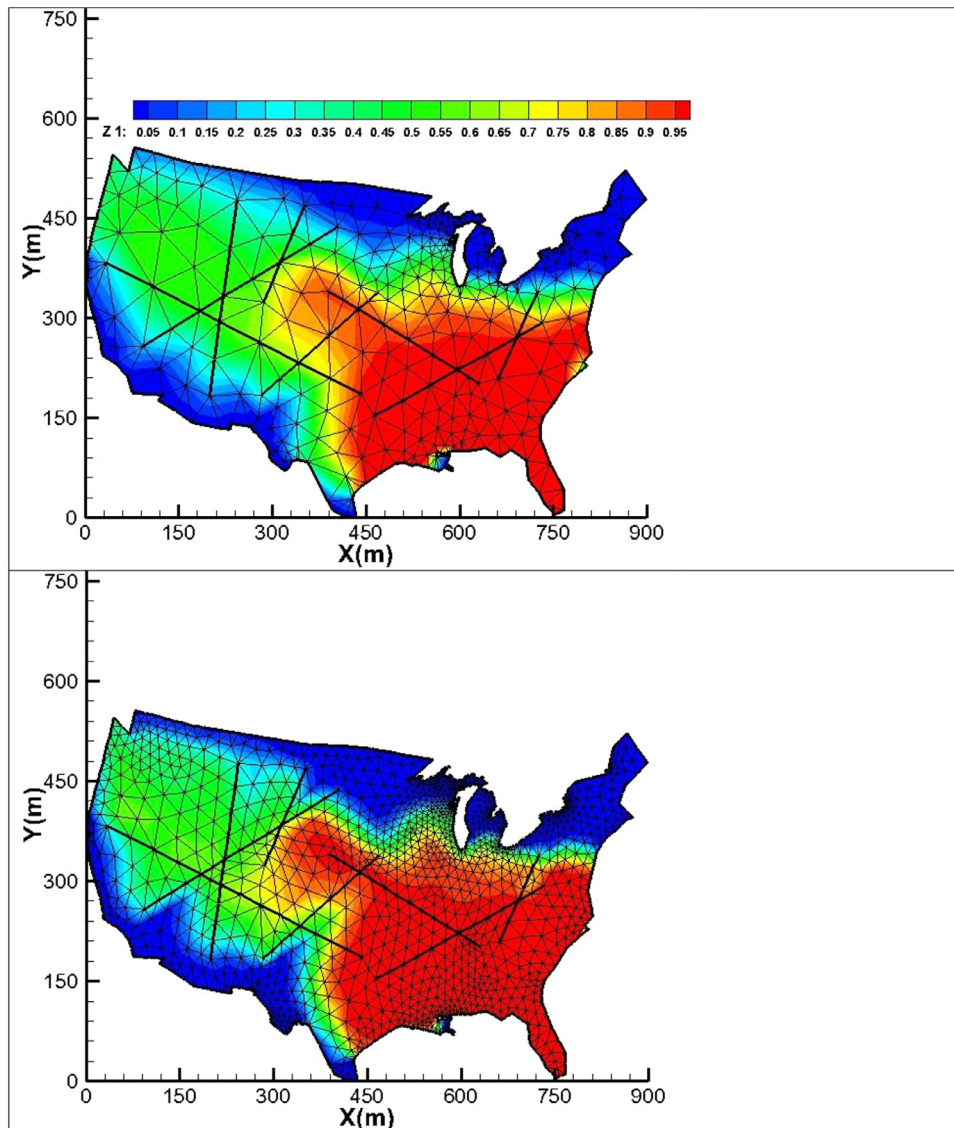


Fig. 17. Overall mole fraction of CO<sub>2</sub> at 50% PVI with 600 elements (a) and 2600 elements (b): Example 5.

#### 6.4. Example 4: 1-Km long domain

In this example we consider a  $1000\text{ m} \times 300\text{ m}$  domain (Fig. 11) with a set of randomly distributed fractures with lengths from 220 m to 350 m. We run this example in five different mesh refinements (Fig. 11) going from a very coarse mesh of 75 elements to 1600 elements. The properties of the domain are the same as in Example 3 except a 1 mm fracture thickness is used. Injection well is located at one corner with a constant rate of 1 PV/year, and production is performed at constant pressure at the opposite corner. In Figs. 12 and 13, we show the overall mole fraction of methane at 10 and 60% PVI with all meshes. Results show that even with the coarse mesh of 600 elements, the model produces comparable results to the relatively fine mesh of 1600 elements at low and high PVI. The high accuracy of our model is partly due to the higher-order nodal discontinuous Galerkin method. In nodal DG, one node connects more information with the surrounding elements compared to the lower-order FV method. In the latter, one grid-cell shares the same average value with the surrounding three elements at the edges

of the triangular finite element. For a more qualitative study of the mesh refinement we compare the overall mole fraction of methane at the production well in all meshes (Fig. 14). A good agreement is observed starting from a 300 elements compared to the 1600 mesh. The CPU time is 4 min for 1600 refined mesh. We run a simulation with 3200 elements for this problem (not shown) and results are in agreement with the results of 1600 element mesh.

#### 6.5. Example 5: Non-regular boundaries

In the previous examples we considered rectangular domains, although the discretization is based on unstructured grids. In such cases, where there is no complexity in geometry, the use of our CAD interface is not needed. When the geometry becomes more complex, the use of our CAD interface becomes essential for efficient mesh generation. In this example we consider a complicated domain boundaries as shown in Fig. 15a. The domain is generated using the CAD interface that was discussed above. The domain includes a set of randomly distributed frac-

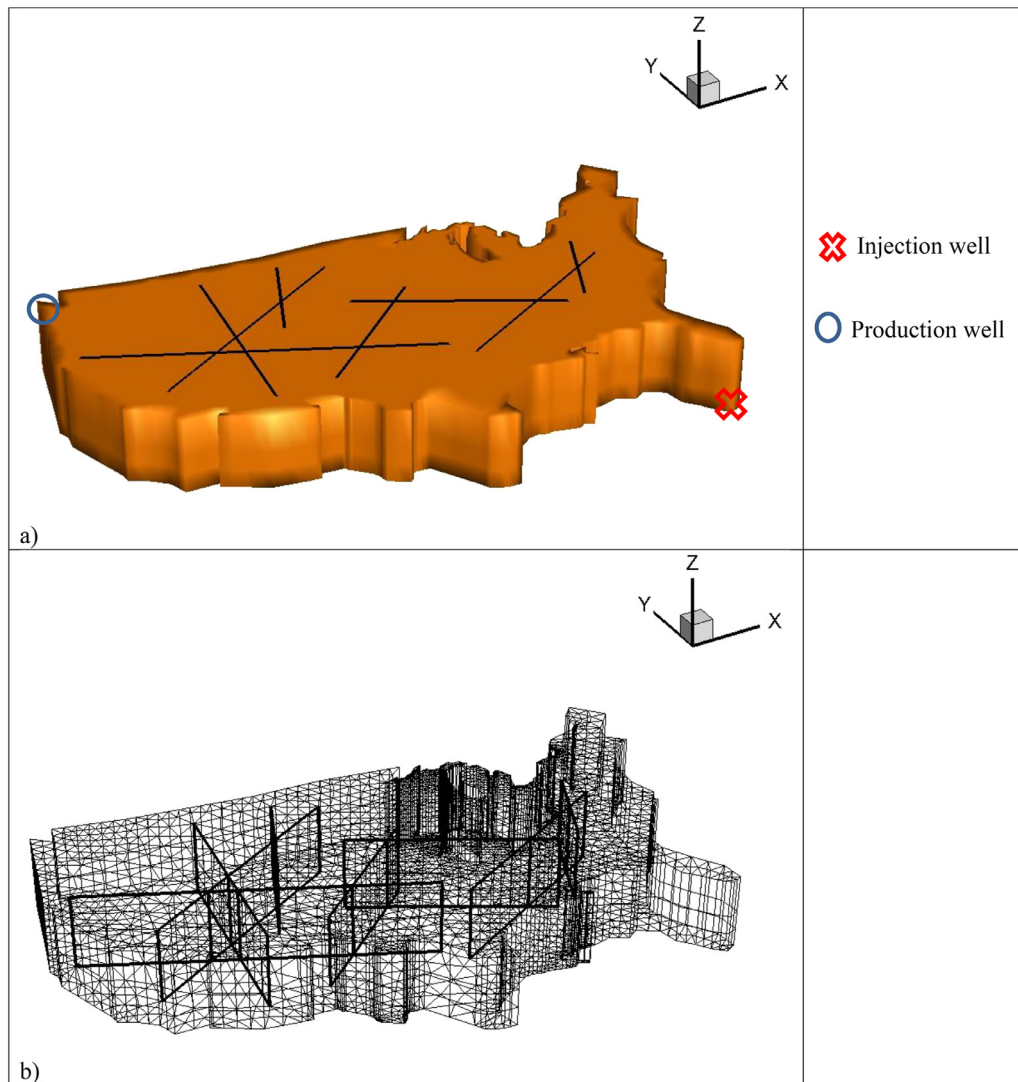


**Fig. 18.** Domain with locations of injection and production wells (a), and mesh (b) (thick black lines represent the fractures; domain size is the same as Example 5 with 100 m vertical extrusion): Example 6.

tures with different lengths varying from 140 to 460 m.  $\text{CO}_2$  is injected at one corner to displace propane to the opposite corner of the domain. The locations of the injection and production wells are shown in Fig. 15a. The relevant data of the domain is shown in Table 3. Two different mesh refinements are used: a coarse mesh of 600 elements and a fine mesh of 2600 elements (Fig. 15b,c). The overall mole fraction of  $\text{CO}_2$  at 10% and 50% PVI is shown in Figs. 16 and 17, respectively, for both meshes. There is good agreement.

As shown in Fig. 15, the largest elements in the computational domain are located near the fracture network. This advantage of the FCFE approach results in: (i) lower total number of elements, and (ii) avoiding the excessive CFL condition in and near the fractures. Away from the fracture network the size of the elements reduces as a result of the complex boundaries and not as a requirement by the model. In a domain with complex boundaries, the small areas are discretized with smaller finite elements. In this example these areas are located between 450 and 750 m (shown by dashed circles in Fig. 15c). Having a coarser mesh in these areas is possible but will result in losing details of the meanders at the boundaries. The CPU time for the refined mesh is 8 min.

#### 6.6. Example 6: 2.5D vertical extrusion of the 2D complex domain

The CAD interface in our mesh generator help with the generation of complicated 3D domains. In this example the domain of the previous example is extruded in the z-direction with a thickness of 100 m (Fig. 18a). The properties of the domain in this example are the same as in Example 5. Locations of the injection and production wells are shown in Fig. 18a. The mesh is based on the refined mesh of Example 5 (2600 elements, see Fig. 15c). The 2D mesh is then extruded into 3 layers; 2 layers of 25 m thickness and a third layer at the top of 50 m thickness. The fractures that are represented by lines in 2D are now represented by planes in 3D. The mesh of the domain with the fractures is shown in Fig. 18b. Extruding a triangular finite element into a 3D space creates a prism FE. The prism FE offers the same flexibility as the triangular FE offers in 2D. The prism could be rotated in a way that one (or more) of the interfaces is (are) aligned with the desired locations of the fractures. In Figs. 19 and 20 we show the overall mole fraction of  $\text{CO}_2$  in the matrix (Figs. 19a, 20a) and in the fracture network (Figs. 19b, 20b) at 10%

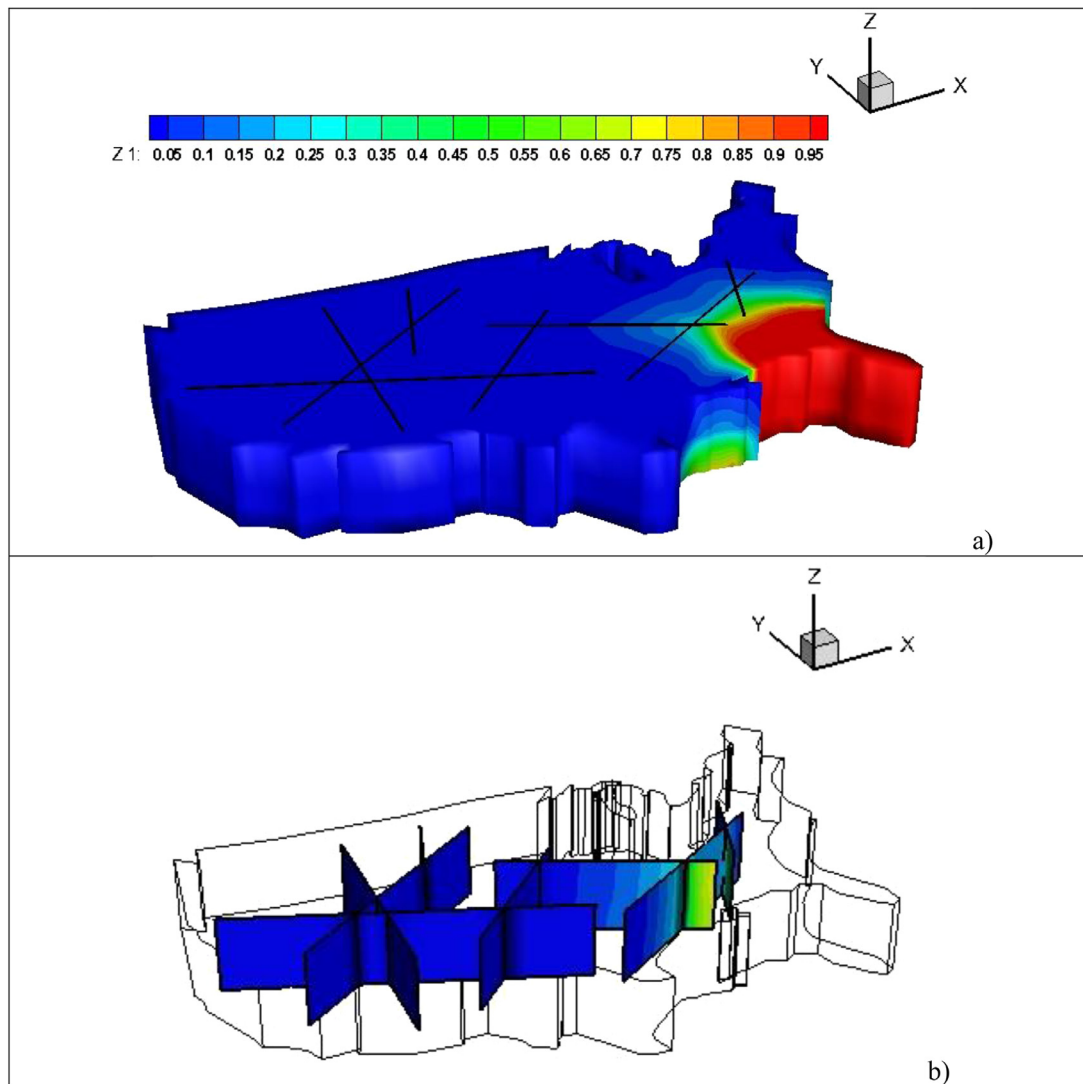


Fig. 19. Overall mole fraction of CO<sub>2</sub> in matrix (a) and in fractures (b) at 10% PVI (domain size is the same as Example 5 with 100 m vertical extrusion): Example 6.

and 50% PVI, respectively. The CPU time to 1 PVI in this example is 45 min.

6.7. Example 7: Fractured sandwich reservoir

In the last example we consider a multilayered fractured reservoir with 1 Km long, 0.3 Km width and 0.3 Km height (Fig. 21a to d). As shown in Fig. 21, the fractures have different orientations along the x and y axes. The reservoir consists of four overlapped layers; two layers have a permeability of 0.1 md and a porosity of 10% and two layers with 10 md and a porosity of 20%. The layers are arranged as shown in Fig. 21-e. The mesh and the location of the fractures are shown in Fig. 21-f. The properties of the domain are given in Table 4. The total number of elements in the matrix domain and the fracture network are 6000 and 600, respectively. The composition of the initial oil is shown in Table 5. CO<sub>2</sub> is uniformly injected at one vertical side and production is performed uniformly at the opposite vertical side of the domain. For reference, we show the overall mole fraction of the injected CO<sub>2</sub> at 15, 25 and 80% PVI in both the matrix domain and the fracture network (Fig. 22). The high value of mole

fraction of the injected fluid at the top and the low value at the bottom, even at 80% PVI, are due to two factors: (i) the difference in matrix permeability between top and bottom, and (ii) the effect of the boundary meanders on flow. The CPU time in this example is about 28 min.

7. Summary and conclusions

We have incorporated the FCFE concept in 2D, 2.5D and 3D unstructured grids to simulate multicomponent compressible flow in fractured media. Our grid generator is coupled with a CAD interface. Based on the results from the examples in the text and in the appendices we draw the following conclusions:

- One can readily adapt the MFE formulation to simulate anisotropic and heterogeneous media. The mixed finite element (MFE) formulation can be readily adapted to account for full permeability tensors to simulate anisotropic and heterogeneous media.



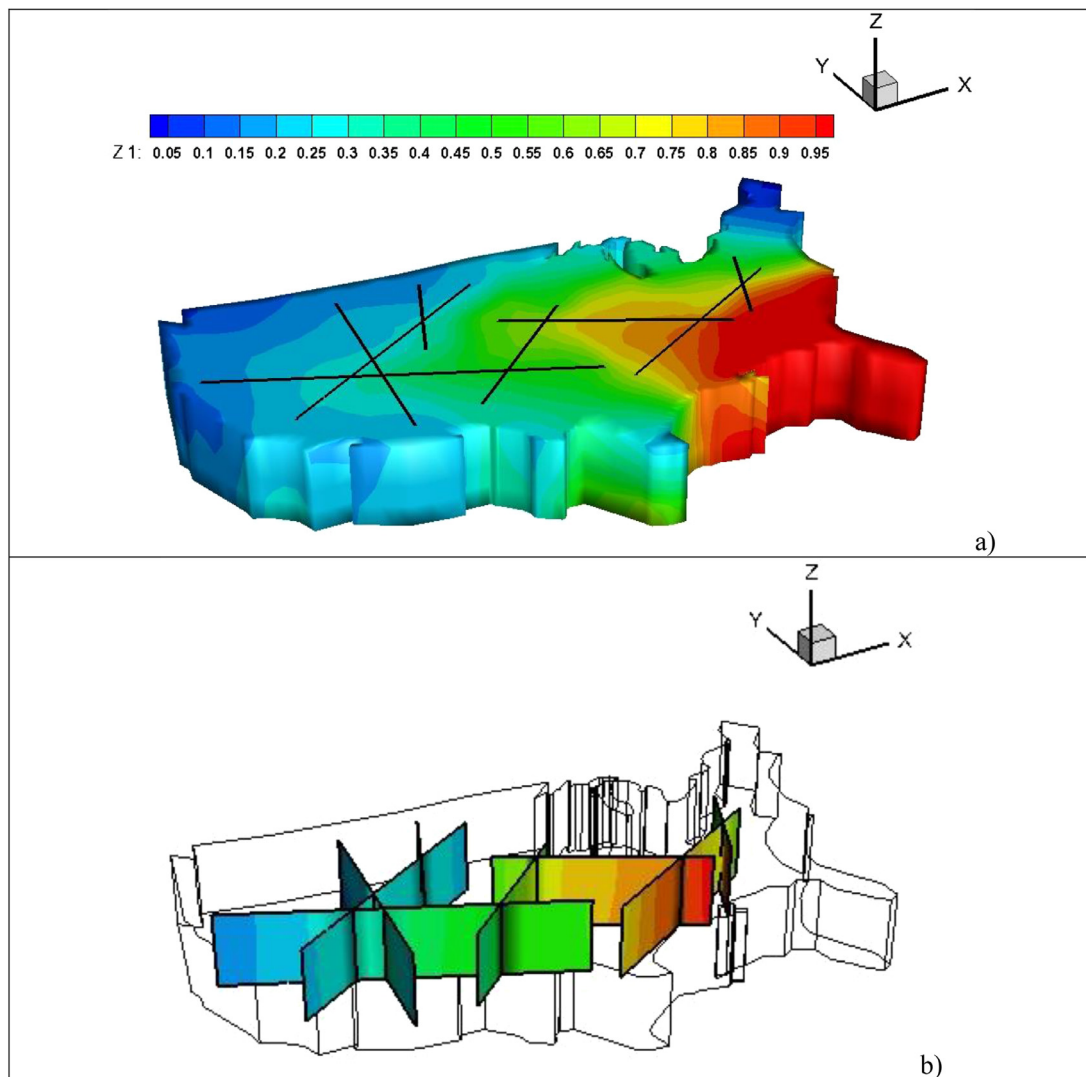


Fig. 20. Overall mole fraction of  $\text{CO}_2$  in matrix (a) and in fractures (b) at 50% PVI (domain size is the same as Example 5 with 100 m vertical extrusion): Example 6.

- We demonstrate that the incorporation of the FCFE concept with higher-order DG alleviates the need for mesh refinement in complicated domains in unstructured gridding.
- The prism and tetrahedra FE with FCFE in 3D allow simulation of realistic fractured domains. The extrusion of prism FE from 2D triangular elements makes the fracture entities in 3D to be represented by planes. As a result one could have the fractures oriented with different angles along the three axes, and removes the limitation on the number of intersecting fractures as opposed to hexahedron FE.
- Accuracy of the algorithm is demonstrated by convergence of coarser mesh to the results of a more refined mesh even in complicated geometries.
- The use of a CAD interface is found to be a very efficient way to generate complex geometries in 2D and 3D.
- Unstructured tetrahedron FE allows simulation of domains that include sharp boundaries in physical properties as in the case of pinch-out problems.

Application of our CAD interface to fractures in fully unstructured gridding is limited in this work to planar fracture shapes. When the

fracture shapes are more complex coupling with CAD is challenging. This will be investigated in the future.

The work covers single phase flow in 2D and in 3D. A full extension to multiphase compositional flow adds more complexity to the formulation and the computational time on unstructured 3D gridding. The surface tension in compositional multiphase flow is low, which reduces the effect of capillary pressure; however, more complexity arises when calculating the matrix-fracture and fracture-fracture exchange flux in different phases; since phase fluxes could be in different directions from matrix to fractures and vice versa. As opposed to single phase flow, in multiphase compositional flow, the implicit solution of the transport equation in the fractures requires the calculation of derivatives of the molar density of each component in each phase with respect to the total molar density of each component. When applied in unstructured grid in 2D and/or 3D, these derivatives should be calculated for all intersected fractures. In single phase flow this derivative is always one. Full coupling of the CAD to unstructured tetrahedron FE and adding multiphase compositional flow to unstructured 2D and 3D grids is in progress for future publication.

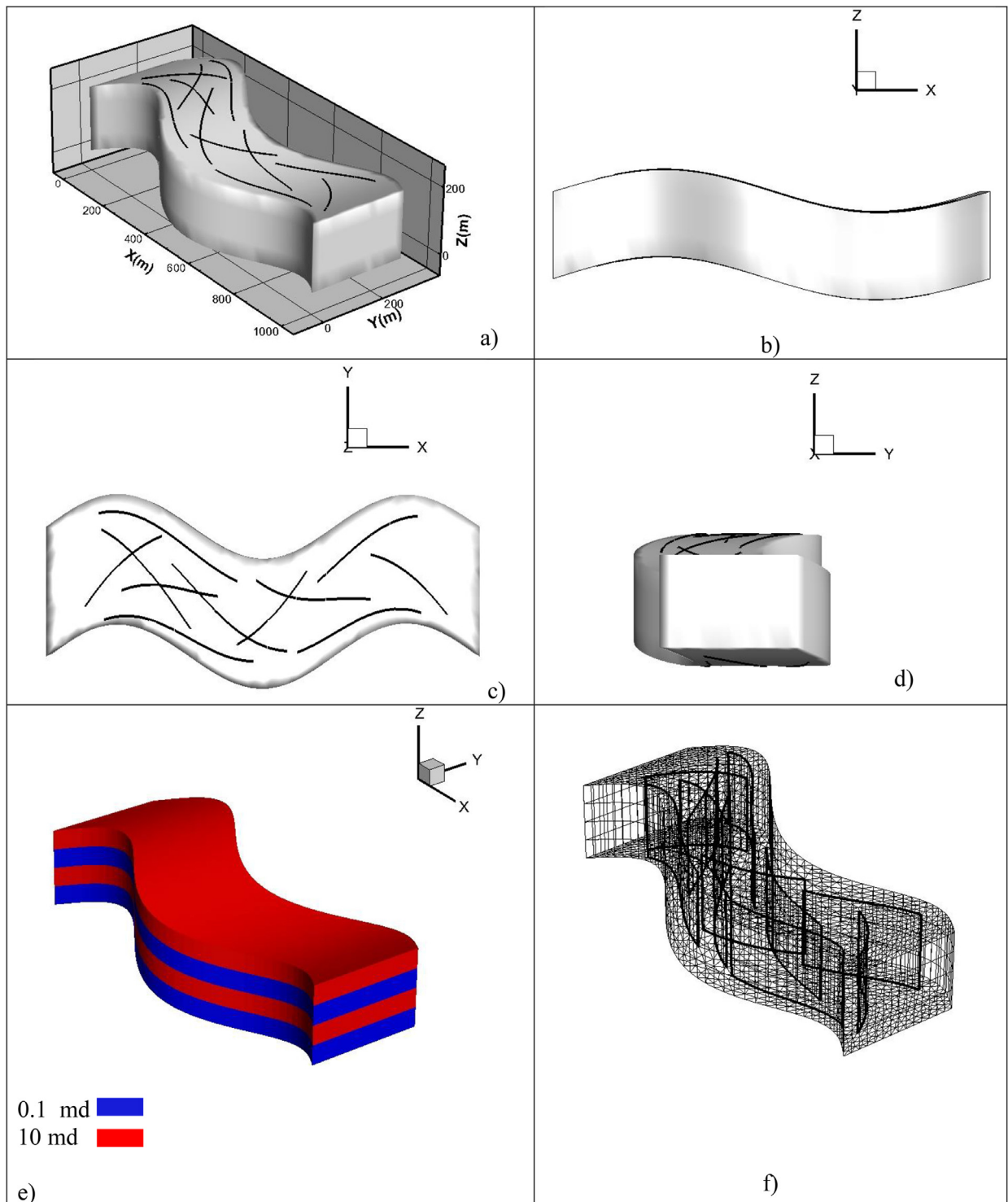


Fig. 21. Domain and 3D mesh (fractures are represented by thick black lines) domain dimensions (a), x-z projection (b), x-y projection (c), y-z projection (d), permeability layers (e) and mesh (f): Example 7.

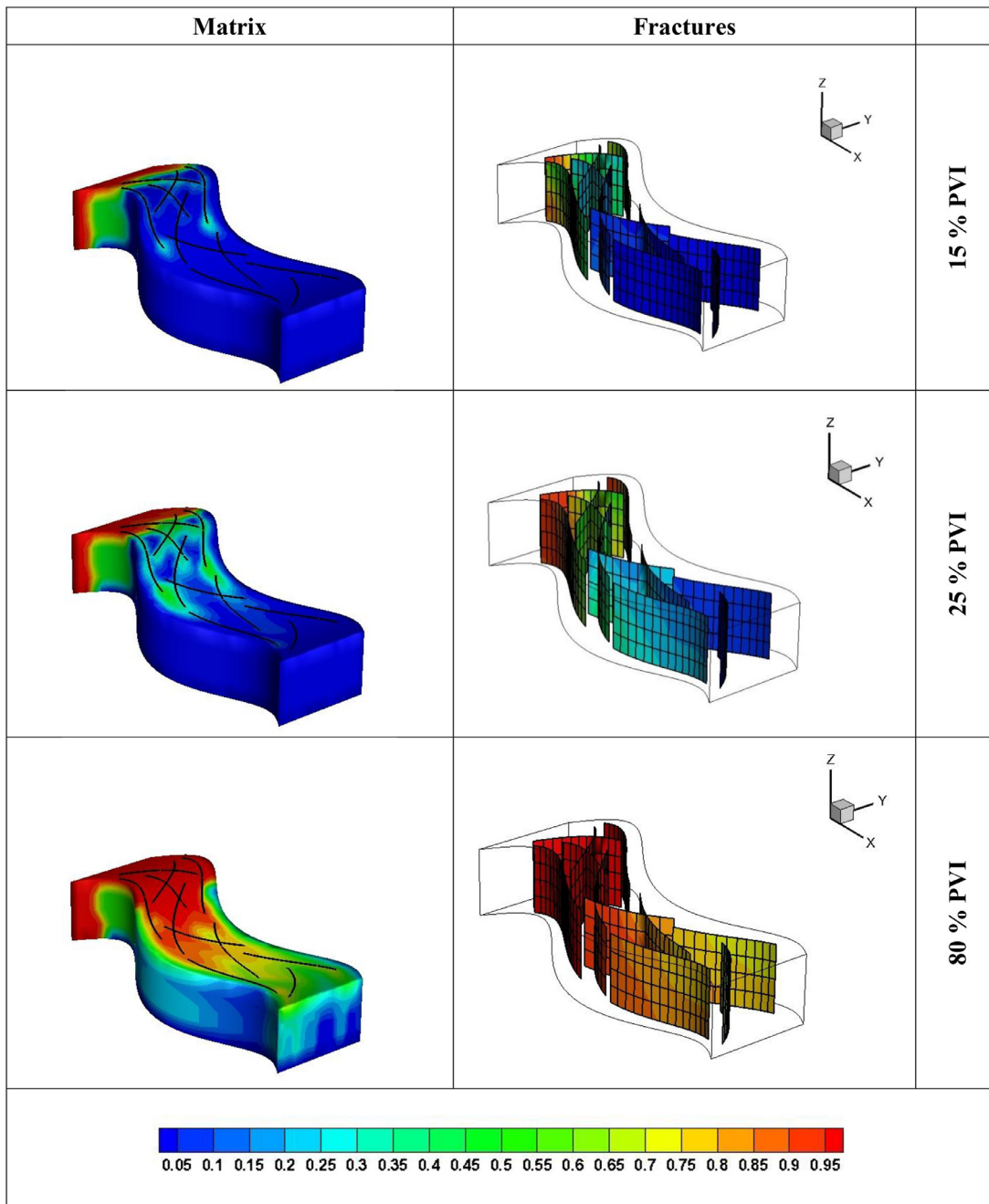


Fig. 22. Overall mole fraction of CO<sub>2</sub> at different PVIs in the matrix domain (left) and the fracture network (right), (domain size 1000 × 300 × 300 m<sup>3</sup>): Example 7.

**Acknowledgement**

This work was supported by the member companies of the Reservoir Engineering Research Institute (RERI) whose support is gratefully acknowledged.

**Appendix A. Discretization of the pressure equation**

In this appendix we show how to obtain the global system of equations to solve for the pressure.

The continuity of the fluxes and the pressure at the interfaces in the matrix domain leads to:

$$\begin{bmatrix} R^{T,m,m} \\ R^{T,m,f} \end{bmatrix} [P^m] - \begin{bmatrix} M^{m,m} & M^{m,f} \\ M^{f,m} & M^{f,f} \end{bmatrix} \begin{bmatrix} T P^m \\ P^f \end{bmatrix} = \begin{bmatrix} 0 \\ Q^f \end{bmatrix} \tag{11}$$

And in the fracture network:

$$[R^{T,f}] [P^f] - [M^f] [T P^f] = [0] \tag{12}$$

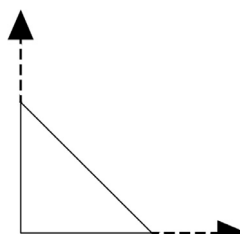
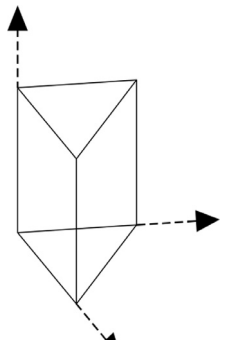
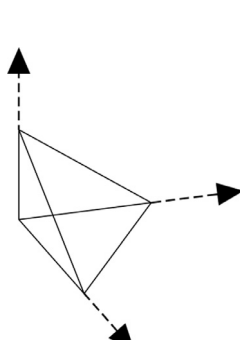
Integration of the pressure equation (Eq. 6 in the text) in the matrix gives:

$$[\bar{D}^m] [P^m] - [\bar{R}^{m,m} \ \bar{R}^{m,f}] \begin{bmatrix} T P^m \\ P^f \end{bmatrix} = [F^m] \tag{13}$$

**Table A1**  
Elements in matrices of the pressure equations.

Matrix	Elements
$\alpha_{K,E}$	$\sum_{E'} \beta_{K,E,E'}$
$\beta_{K,E,E'}$	$(B_K^{-1})_{E,E'}$
$B_{K,E,E'}$	$f_k w_{K,E} K^{-1} w_{K,E'}$
$R^{T,m,m}$	$\alpha_{K,E}^m$
$R^{T,m,f}$	$\alpha_{K,E}^m$
$M^{m,m}$	$\sum_{E' \in \partial K} \beta_{K,E,E'}^m$
$M^{m,f}$	$\sum_{E' \in \partial K} \beta_{K,E,E'}^m$
$M^{f,f}$	$\sum_{E' \in \partial K} \beta_{K,E,E'}^m$
$A^{m,m}$	$R^{T,m,m} D^{m-1} \hat{R}^{mm} - M^{m,m}$
$A^{m,f}$	$R^{T,m,m} D^{m-1} \hat{R}^{mf} - M^{m,f}$
$A^{f,m}$	$-R^{T,m,f} D^{m-1} \hat{R}^{mm} + M^{f,m}$
$A^{f,f}$	$-R^{T,m,f} D^{m-1} \hat{R}^{mf} + M^{f,f} + D^f$
$V^m$	$-R^{T,m,f} D^{m-1} G^m$
$V^f$	$G^f + R^{T,m,f} D^{m-1} G^m$
$D^m$	$\frac{\phi_{C1}  K }{\Delta t} + \alpha_{K,E}^m$
$G^m$	$\frac{\phi_{C1}  K }{\Delta t} p_K^i + \sum_i \bar{V}_i  K  F_i$

**Table A2**  
Basis functions for DG and RT in different FEs.  
The basis functions for DG ( $\varphi$ ) and RT ( $w$ ) for different FEs are given below:

Reference element	DG	RT
	$\varphi_1 = 1 - x - y$ $\varphi_2 = x$ $\varphi_3 = y$	$w_1 = \begin{pmatrix} x \\ y - 1 \end{pmatrix}$ $w_2 = \begin{pmatrix} x \\ y \end{pmatrix}$ $w_3 = \begin{pmatrix} x - 1 \\ y \end{pmatrix}$
	$\varphi_1 = (1 - x - y)(1 - z)$ $\varphi_2 = x(1 - z)$ $\varphi_3 = y(1 - z)$ $\varphi_4 = (1 - x - y)z$ $\varphi_5 = xz$ $\varphi_6 = yz$	$w_1 = \begin{pmatrix} x \\ y - 1 \\ 0 \end{pmatrix}$ $w_2 = \begin{pmatrix} x \\ y - 1 \\ 0 \end{pmatrix}$ $w_3 = \begin{pmatrix} x \\ y \\ 0 \end{pmatrix}$ $w_4 = 2 \begin{pmatrix} 0 \\ 0 \\ z \end{pmatrix}$ $w_5 = 2 \begin{pmatrix} 0 \\ 0 \\ z - 1 \end{pmatrix}$
	$\varphi_1 = 1 - x - y - z$ $\varphi_2 = x$ $\varphi_3 = y$ $\varphi_4 = z$	$w_1 = 2 \begin{pmatrix} x \\ y - 1 \\ z \end{pmatrix}$ $w_2 = 2 \begin{pmatrix} x \\ y \\ z \end{pmatrix}$ $w_3 = 2 \begin{pmatrix} x \\ y \\ z \end{pmatrix}$ $w_4 = 2 \begin{pmatrix} x \\ y \\ z - 1 \end{pmatrix}$

And in the fractures

$$[\bar{D}^f] [P^f] - [\bar{R}^f] [T P^f] = [F^f] + [Q^f] \tag{14}$$

Combining the above equations and using the Gaussian elimination to reduce the size of the global system we get:

$$\begin{bmatrix} A^{m,m} & A^{m,f} & 0 \\ A^{m,f} & A^{f,f} & -\bar{R}^f \\ 0 & R^{T,f} & M^f \end{bmatrix} \begin{bmatrix} T P^m \\ P^f \\ T P^f \end{bmatrix} = \begin{bmatrix} V^m \\ V^f \\ 0 \end{bmatrix} \tag{15}$$

The elements of the matrices in the above equations are given in Table A1. The coefficient  $w_{K,E}$  in Table A1 are the Raviart–Thomas basis functions and  $K$  is the permeability tensor (see Zidane and Firoozabadi, 2014). In Table A1  $E$  represents the edge where the parameters ( $\alpha_{K,E}$ ,  $\beta_{K,E,E'}$ ) are evaluated and  $E'$  represents the adjacent edges of  $E$  in the element  $K$ .

**Appendix B. Matrix and fractures discretization variables and exchange fluxes**

We adopt a lower dimensional representation of the fractures compared to the matrix dimension. This is justified because of small fracture aperture compared to the matrix domain. Each fracture element exchanges fluxes with two matrix elements. The two fluxes ( $\bar{Q}_i^{f,K_1} + \bar{Q}_i^{f,K_2}$ ) belong to the interfaces of the matrix grid cells. If the fracture element is at the boundary of the domain, the interaction in this case is limited to one matrix element. Therefore, three different scenarios could be observed regarding the matrix-fracture flux. The first case is when the two matrix elements are feeding the fracture element (represented by fracture  $f_1$  in Fig. B1). The second case is when the fracture is feeding the adjacent two matrix elements (represented by fracture  $f_2$  in Fig. B1). The last case when one matrix element is feeding the fracture and the latter is feeding the adjacent matrix element (fracture  $f_3$  in Fig. B1).

The effect of the three scenarios in the numerical discretization follows. In the first case (fracture  $f_1$ ), both fluxes ( $\bar{Q}_i^{f,K_1}$ ,  $\bar{Q}_i^{f,K_2}$ ) are treated explicitly in the temporal scheme. In the second case (fracture  $f_2$ ), both fluxes ( $\bar{Q}_i^{f,K_3}$ ,  $\bar{Q}_i^{f,K_4}$ ) are treated implicitly. In the last case, one flux is treated implicitly ( $\bar{Q}_i^{f,K_4}$ ) and one flux is treated explicitly ( $\bar{Q}_i^{f,K_5}$ ). In the implicit treatment, the flux is added to the updated Newton–Raphson (NR) iteration, and in the explicit treatment the flux is added to the residual function in the NR iteration. The flow and transport variables are represented by different symbols in Fig. B1.

**Appendix C. Pinch-out problem**

Subsurface formations are generally complex. Structured grid cells and/or grids that are based on the concept of pillars, may not describe complex formations. Description of pinch-outs is a clear example of the limitations of Cartesian grids. In our algorithm, to simulate complex systems, the unstructured tetrahedra are natural choices. We show in Fig. C1 a domain of 30 Km long, 20 Km wide and 10 Km height. We consider a pinched-out impermeable layer in the domain. The exact location of the impermeable layer is shown in Fig. C1.

We inject of CO<sub>2</sub> along one vertical side of the domain and production is performed at the opposite vertical side. All properties of the problem are the same as in Example 7. For reference we show in Fig. C4 the overall mole fraction of CO<sub>2</sub> at different PVI. For simplicity we consider a no-gravity scenario. The CPU time to 1 PVI is 8 min with a total of 4500 elements.

**Appendix D. Oblique fracture**

The modeling of unstructured tetrahedra is not limited to pinch-out problems. One important application is the modelling of oblique fractures. In this appendix we show the application of FCFE in unstructured

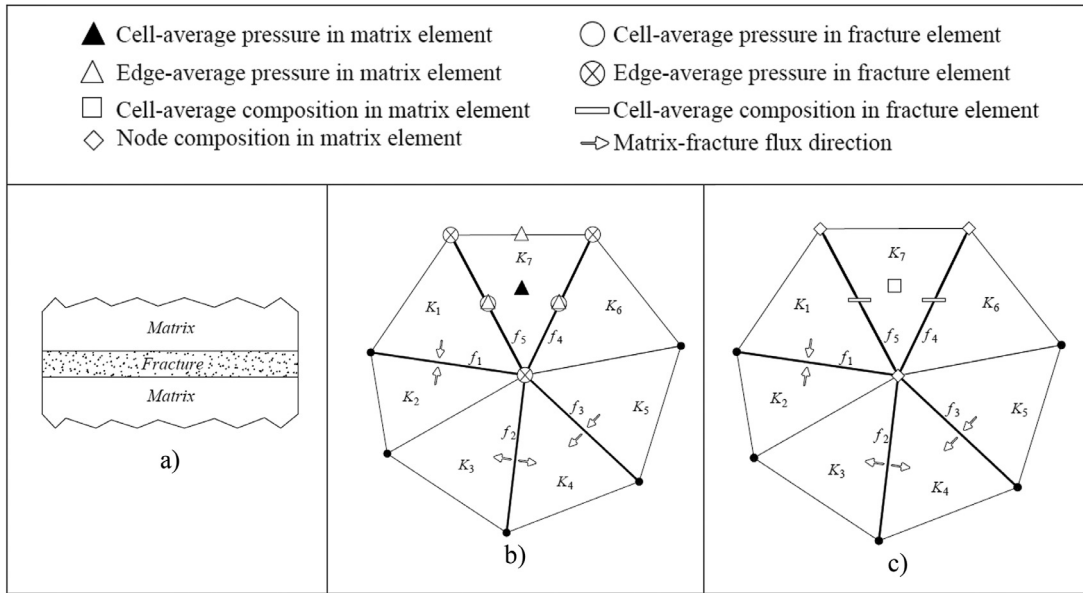


Fig. B1. Physical domain of one fracture (a); flow discretization of domain with five intersecting fractures (b), transport discretization of domain with five intersecting fractures (c) (thick lines represent fracture elements).

tetrahedra. We consider the oblique fracture shown in Fig. D1 in a domain of 12 Km long, 5 Km wide and 5 Km height. To model such oblique fractures, the use of unstructured tetrahedra is a necessity. The application of CAD to unstructured tetrahedra with fractures is limited to planar fracture shapes. When the fracture shapes become more complex coupling CAD with unstructured tetrahedra is more challenging. This will be investigated in future.

CO<sub>2</sub> is injected at one vertical side and production is at the opposite vertical side of the domain. All properties of the problem are the same as in Example 7. For reference we show the overall mole fraction of CO<sub>2</sub> at different PVIs in Fig. D2. The CPU time for 1 PVI is 13 min with a total of 5500 elements.

**Appendix E. Impermeable fault**

All examples so far demonstrate the applicability of the FCFE in high permeability fractures. The FCFE concept can be readily applied to simulate flow in a domain with barriers as we present in this example. We consider a 10×10 Km<sup>2</sup> domain and 4 Km height as shown in Fig. E1. The domain has a flow barrier shown in the thick black line (Fig. E1) near the injection well corner. CO<sub>2</sub> is injected at one corner to displace propane toward the production well at the opposite corner at a rate of 0.1 PV/year. The reservoir temperature is at 311 K and the pressure is 69 bar, permeability is 1 md and the porosity is 20%.

Implementation of flow barriers in FCFE is straightforward. This is due to the fact that the FCFE elements are aligned with the interfaces of the matrix elements. By imposing a zero flux for interfaces with barrier index, the flux is redistributed along the rest of matrix interfaces. The mass balance is always guaranteed. This is applied for the two matrix

elements adjacent to the (n-1)-D element with a barrier index. For reference we show the overall mole fraction of injected CO<sub>2</sub> at different PVIs in Fig. E2. With a number of grids of 1500 elements, the CPU time is 5 min.

**Appendix F. Anisotropy and heterogeneity**

In this example we consider a 100 m×50 m domain initially saturated with propane (C<sub>3</sub>). CO<sub>2</sub> is injected at one corner to displace propane toward the production well at the opposite corner at a rate of 1 PV/year. The reservoir temperature is at 311 K and the pressure is 69 bar. We study three different setups that we denote by Examples Fa, Fb and Fc. In the first two setups we choose two permeability tensors such that the first has a higher permeability within the diagonal from the injection to the production well (K1), with an anisotropy ratio of 140:4 at an angle of 27°; in (K2) the angle is -27°:

$$K1 = \begin{pmatrix} 112 & 55 \\ 55 & 32 \end{pmatrix} \quad ; \quad K2 = \begin{pmatrix} 112 & -55 \\ -55 & 32 \end{pmatrix} \quad (1)$$

In the third setup we consider heterogeneous media by assigning a random permeability value to each grid-cell (Fig. F1). Porosity is set to 20% in all setups. The overall mole fraction of CO<sub>2</sub> in the three domains is shown at different pore volume injections (PVIs) in Fig. F2. The effect of the orientation of the shear is apparent between the first two setups. Anisotropy significantly affects the oil recovery. In the first setup where the shear is aligned with the flow direction, breakthrough occurs at 40% PVI (Fig. F3). In the second setup breakthrough is delayed until 70% PVI. The result is more than 50% difference in oil recovery compared to the first setup (Fig. F3). The CPU time is 3 min with a total of 3000 elements.

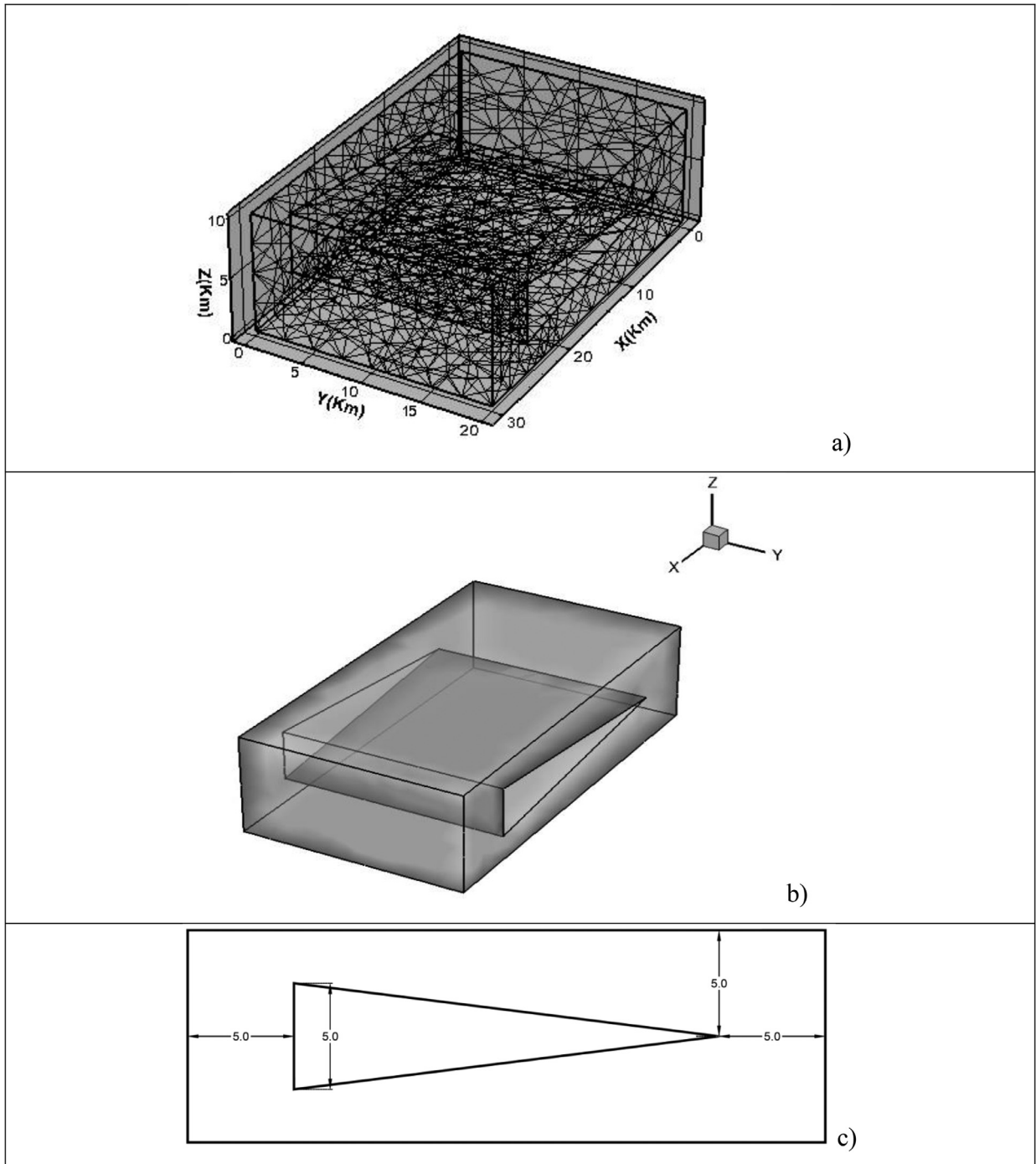


Fig. C1. Discretization with tetrahedra (a); permeable layer of the domain (b) and side view of the impermeable layer (c) (dimensions not to scale).

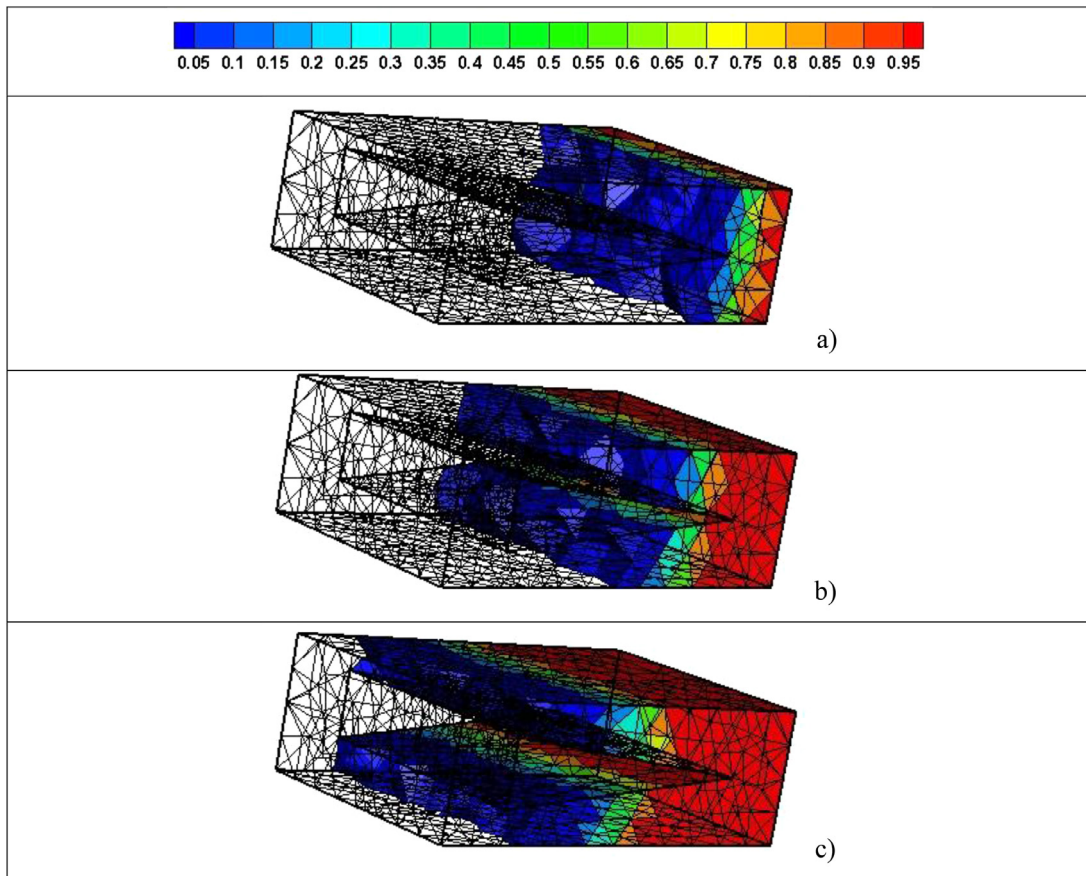


Fig. C2. Overall mole fraction of CO<sub>2</sub> at 10% (a), 40% (b) and 70% (c) PVI (domain size 30 × 20 × 10 Km<sup>3</sup>).

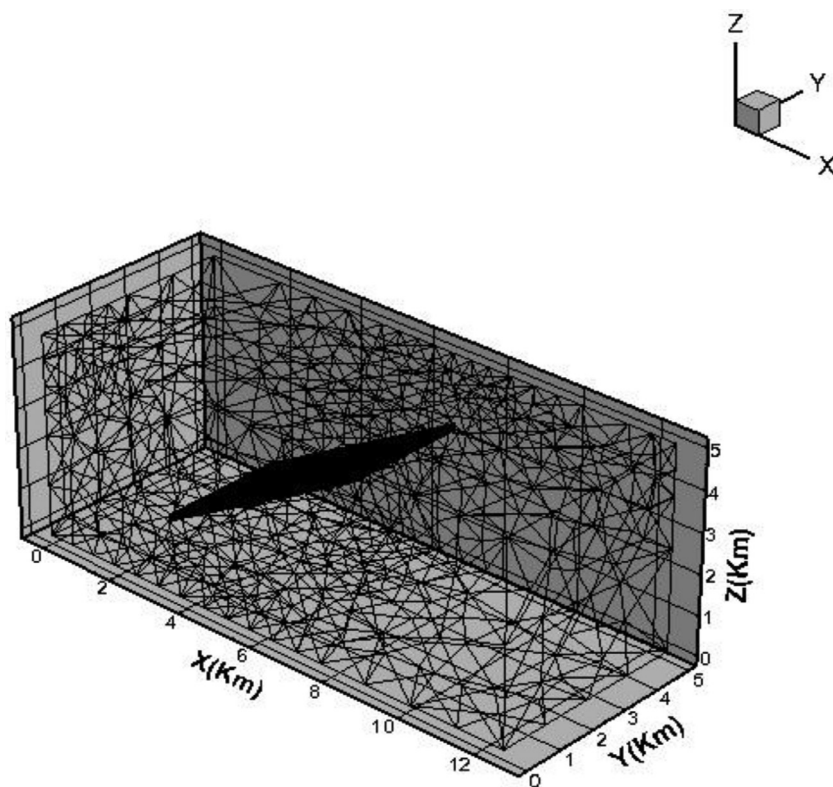


Fig. D1. Domain with oblique fracture (thick black area).

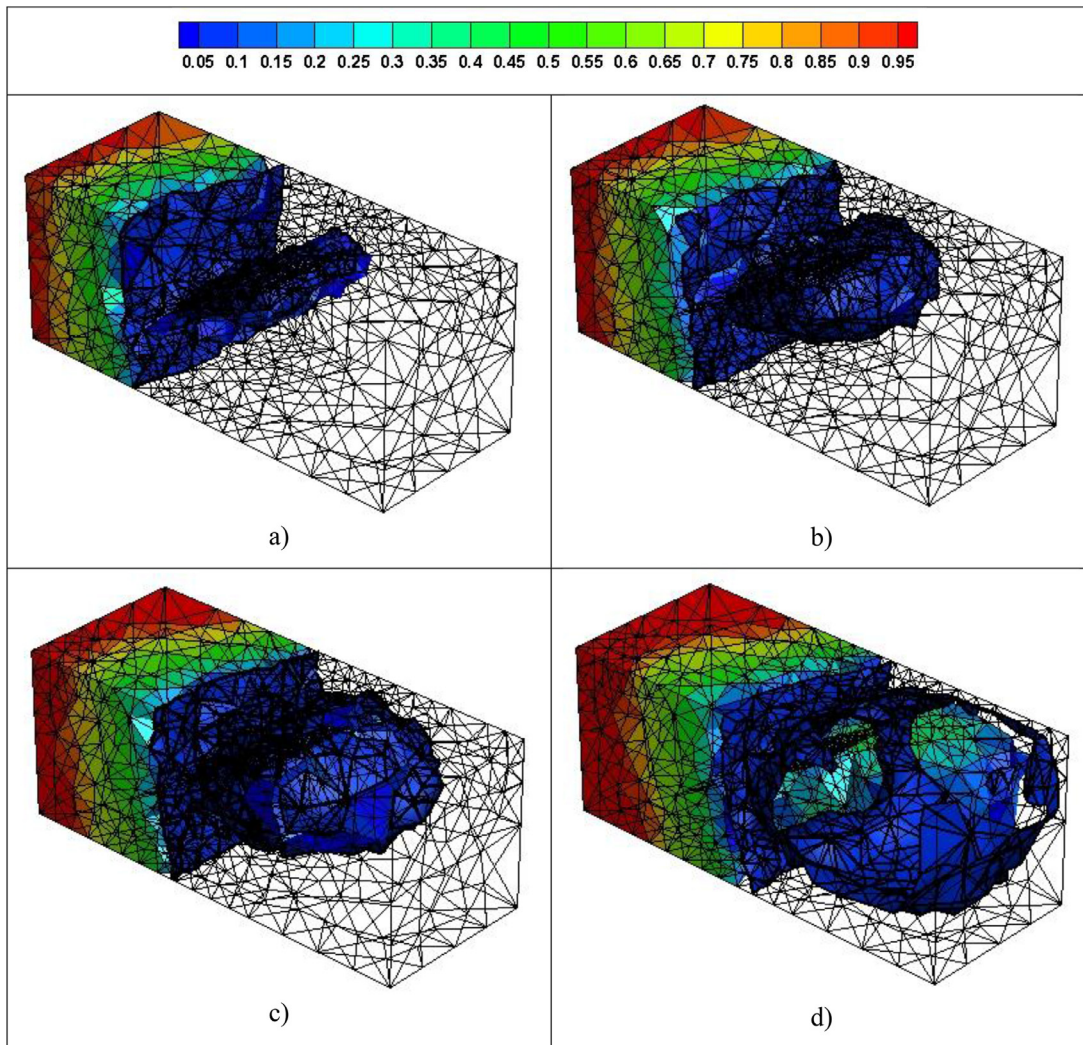


Fig. D2. Overall mole fraction of CO<sub>2</sub> at 35% (a), 45%(b), 55%(c) and 80% (d) PVI (domain size 12×5×5 Km<sup>3</sup>).



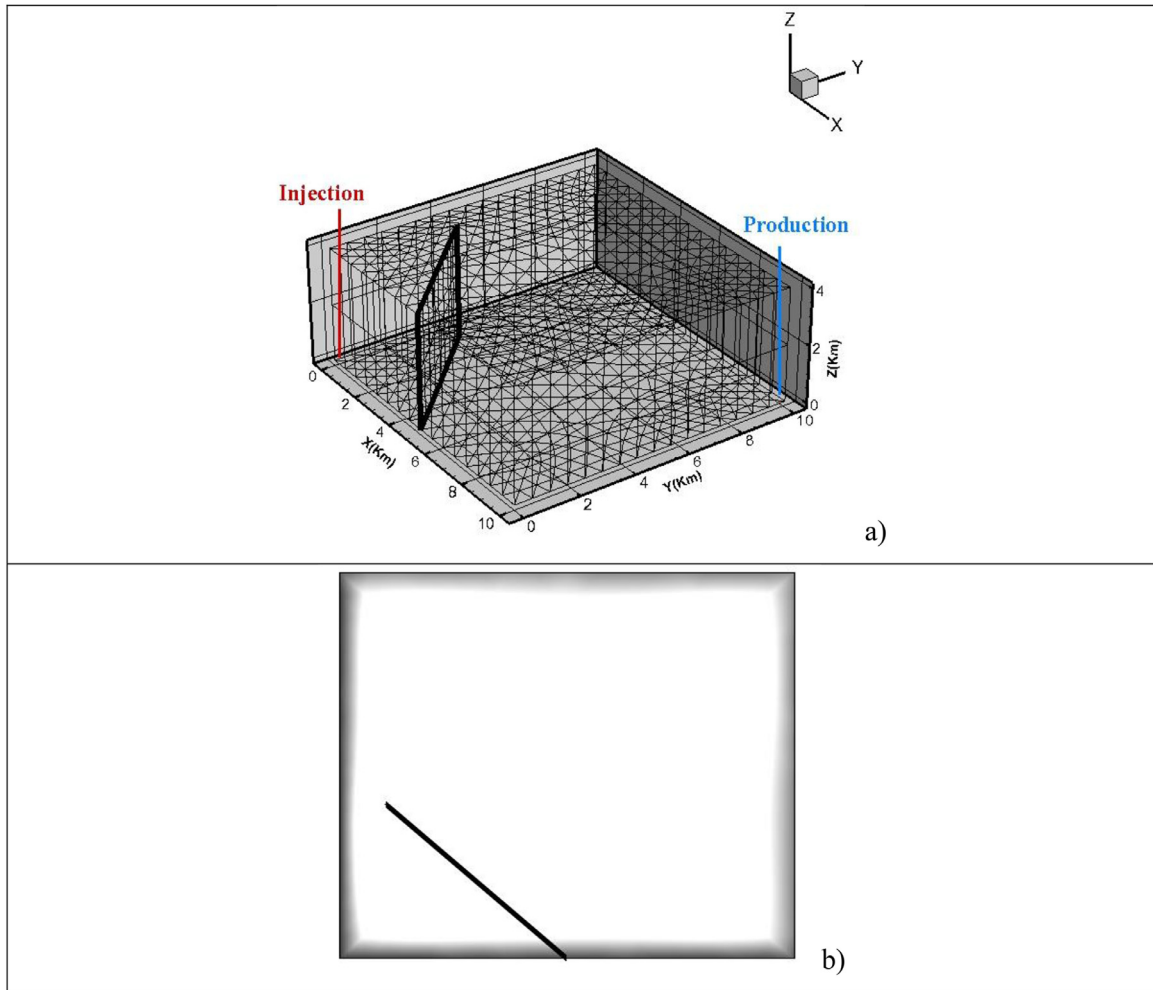


Fig. E1. Domain and barrier shown in thick black line; perspective view (a), and top projection (b).

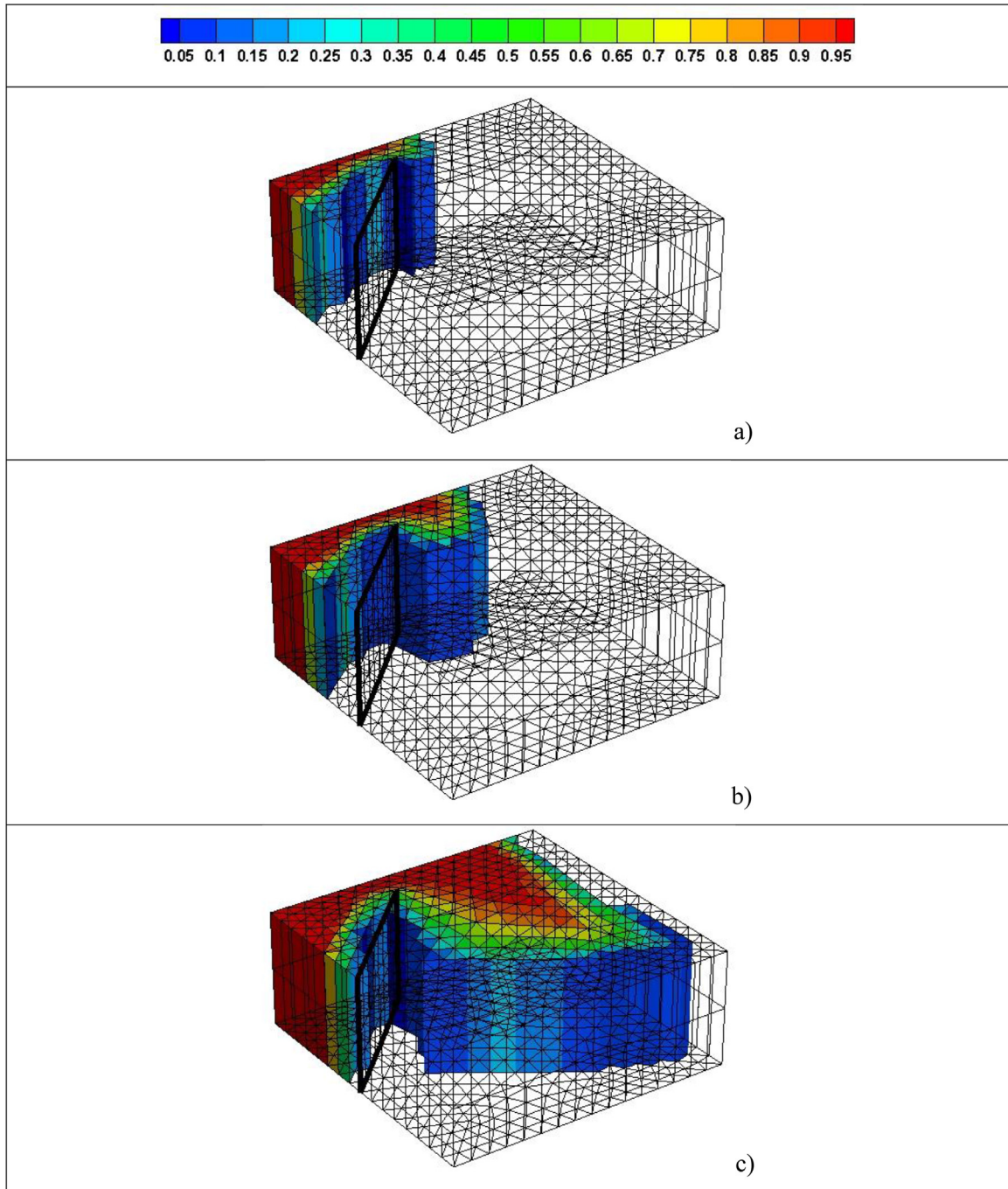


Fig. E2. Overall mole fraction of CO<sub>2</sub> at 10% (a), 20% (b) and 70% (c) PVI (domain size 10 × 10 × 4 Km<sup>3</sup>).

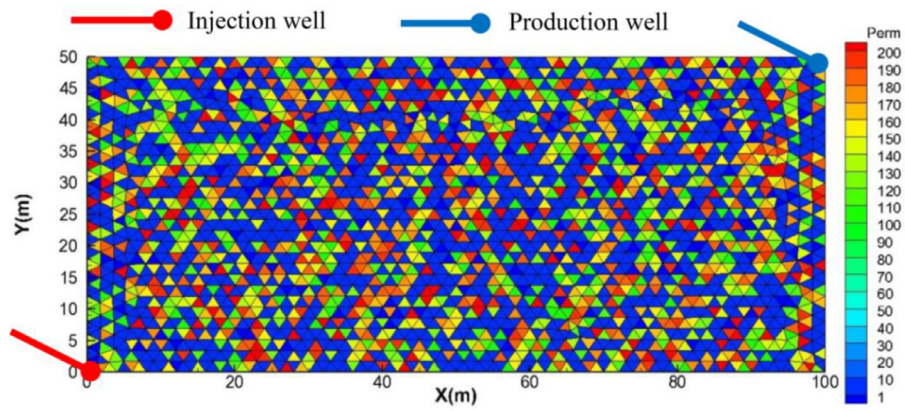


Fig. F1. Random permeability distribution throughout the domain.

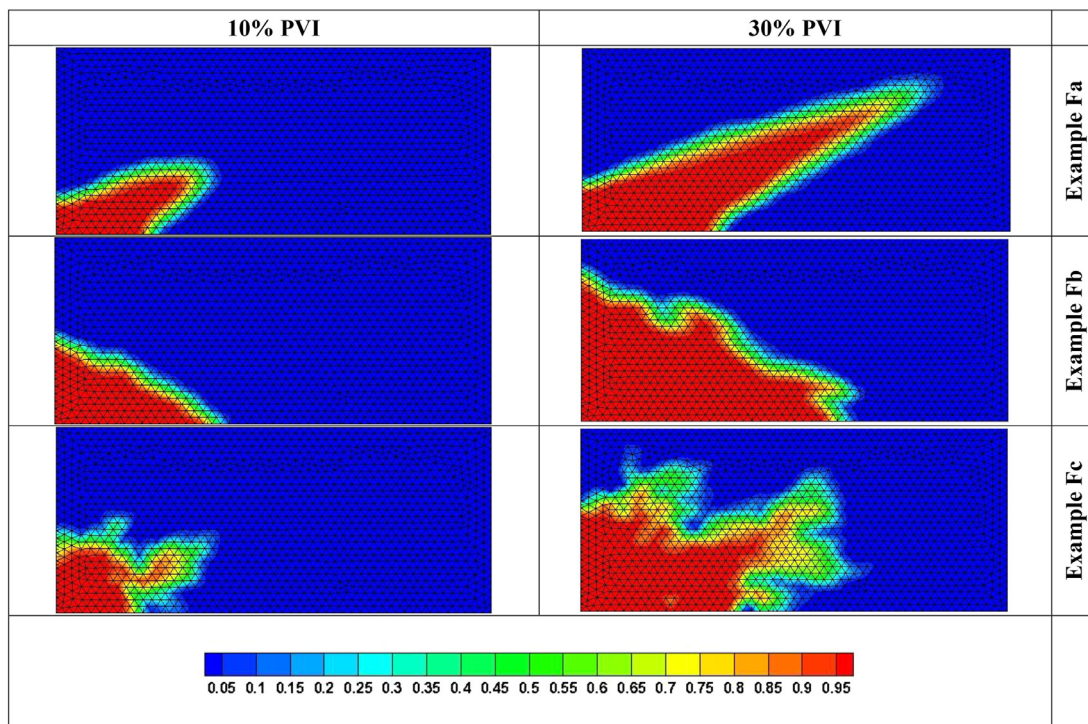


Fig. F2. Overall mole fraction of CO<sub>2</sub> at different PVIs (domain size 100 × 50 m<sup>2</sup>).

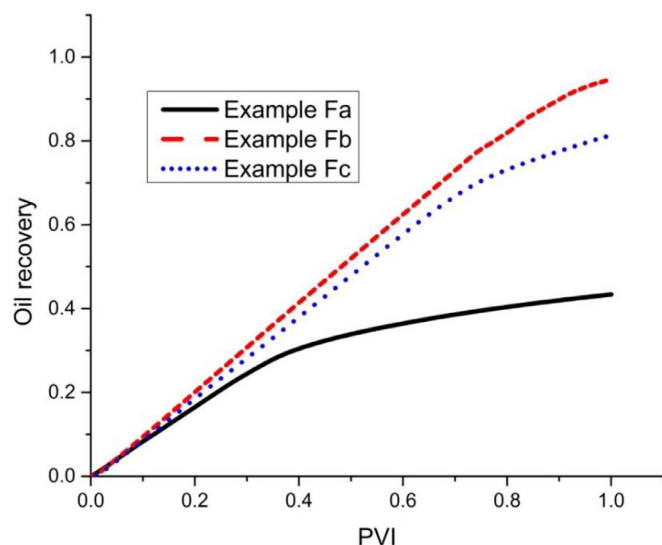


Fig. F3. Oil recovery (fraction) in the three different setups.

## References

- Aavatsmark, I, Barkve, T, Boe, O, Mannseth, T, 1998. Discretization on unstructured grids for inhomogeneous, anisotropic media. Part I: derivation of the methods. *SIAM J. Sci. Comput.* 19, 1700–1716.
- Aavatsmark, I, 2002. An introduction to multipoint flux approximations for quadrilateral grids. *Comput. Geosci.* 6, 405–432.
- Aavatsmark, I, Eigestad, GT, Mallison, BT, Nordbotten, JM, 2008. A compact multipoint flux approximation method with improved robustness. *Numer. Meth. Part D E* 24, 1329–1360.
- Aavatsmark, I, Eigestad, GT, Heimsund, BO, Mallison, BT, Nordbotten, JM, Qian, E, 2010. A new finite-volume approach to efficient discretization on challenging grids. *SPE J.* 15, 658–669.
- Abushaikhaa, A, Blunt, M, Gosselinc, OR, Pain, CC, Jackson, MD, 2015. Interface control volume finite element method for modelling multi-phase fluid flow in highly heterogeneous and fractured reservoirs. *J. Comput. Phys.* <http://dx.doi.org/10.1016/j.jcp.2015.05.024>.
- Acs, G, Doleschall, S, Farkas, E, 1985. General purpose compositional model. *SPE J.* 25 (4), 543–553.
- Ahmed, R, Edwards, MG, Lamine, S, Huisman, BAH, Pal, M, 2015. Control-volume distributed multi-point flux approximation coupled with a lower-dimensional fracture model. *J. Comput. Phys.* 462–489.
- Anderson, W, 1994. A grid generation and flow solution method for the Euler equations on unstructured grids. *J. Comput. Phys.* 110, 23–38.
- Bastian, P, Helmig, R, Jakobs, H, Reichenberger, V, 2000. Numerical simulation of multiphase flow in fractured porous media. In: Chen, Ewing, Shi (Eds.). *Numerical Treatment of Multiphase Flows in Porous Media*, 552. Springer-Verlag, pp. 1–18. editors Lecture Notes in Physics.
- Batista Fernandes, BR, Marcondes, F, Sepehrnoori, K, 2013. Investigation of several interpolation functions for unstructured meshes in conjunction with compositional reservoir simulation. *Numer. Heat Transf. Appl.* 64, 974–993.
- Bogdanov, I, Mourzenko, V, Thovert, J, Adler, P, 2003. Two-phase flow through fractured porous media. *Phys. Rev. E* 68 (2), 1–24.
- Chavent, G, Jaffré, J, 1986. *Mathematical Models and Finite Elements for Reservoir simulation. Studies in Mathematics and its Applications.* Elsevier, North-Holland.
- Chen, J, Tiantai, L, Zhang, Y, 2015. Application of the unstructured grids in the numerical simulation of fractured horizontal wells in ultra-low permeability gas reservoirs. *J. Nat. Gas Sci. Eng.* 580–590.
- Cockburn, B, Shu, C, 1989. TVB Runge–Kutta local projection discontinuous Galerkin finite element method for conservative laws II: general frame-work. *Math Comp* 52, 411–435.
- Cockburn, B, Shu, C, 1998. The Runge–Kutta discontinuous Galerkin method for conservative laws V: multidimensional systems. *J. Comput. Phys.* 141, 199–224.
- Darlow, B, Ewing, R, Wheeler, M, 1984. Mixed finite element method for miscible displacement problems in porous media. *SPE J.* 24, 391–398.
- Di Donato, G, Lu, HY, Taasoli, Z, Blunt, MJ, 2004. Multi-rate-transfer dual-porosity modeling of gravity drainage and imbibition. *SPE J.* 12, 931–944.
- Durlafsky, L, 1994. Accuracy of mixed and control volume finite element approximations to Darcy velocity and related quantities. *Water Resour. Res.* 30 (4), 965–973.
- Edwards, MG., 2002. Unstructured, control-volume distributed, full-tensor finite volume schemes with flow based grids. *Comput. Geosci.* 6, 433–452.
- Edwards, MG, Zheng, H, 2010. Quasi-positive families of continuous Darcy-flux finite volume schemes on structured and unstructured grids. *J. Comput. Appl. Math.* 234, 2152–2161.
- Lamine, S, Edwards, MG, 2013. Higher order cell-based multidimensional upwind schemes for flow in porous media on unstructured grids. *Comput. Methods Appl. M.* 259, 103–122.
- Lamine, S, Edwards, MG, 2010. Multidimensional upwind convection schemes for flow in porous media on structured and unstructured quadrilateral grids. *J. Comput. Appl. Math.* 234, 2106–2117.
- Firoozabadi, A, 2015. *Thermodynamics and Applications of Hydrocarbons Energy Production* McGraw-Hill Professional.
- Fung, LS, Ding, XY, Dogru, AH, 2013. Using unstructured grids for modeling densely-spaced complex wells in field-scale reservoir simulation. In: *Proceedings of the Sixth International Petroleum Technology Conference*, Beijing, China Mar 26–28, Paper SPE-17062-MS.
- Geiger, S, Matthäi, S, Niessner, J, Helmig, R, et al., 2009. Black-oil simulations for three-component, three-phase flow in fractured porous media. *SPE J.* 14 (2), 338–354.
- Geiger, S, Dentz, M, Neuweiler, I, 2013. A novel multirate dual-porosity model for improved simulation of fractured and multiporosity reservoirs. *SPE J.* 18, 670–684.
- Geiger, S, Roberts, S, Matthäi, S, Zoppou, C, Burri, A, 2004. Combining finite element and finite volume methods for efficient multiphase flow simulations in highly heterogeneous and structurally complex geologic media. *GeoFluids* 4 (4), 284–299.
- Gilman, JR, Kazemi, H, 1983. Improvement in simulation of naturally fractured reservoirs. *SPE J.* 23, 695–707.
- Granet, S, Fabrie, P, Lemmonier, P, Quintard, M, 1998. A single phase flow simulation of fractured reservoir using a discrete representation of fractures. In: *Proceedings of the Sixth European Conference on the Mathematics of Oil Recovery (ECMOR VI)* September 8–11, Peebles, Scotland, UK.
- Hoteit, H, Ackerer, P, Mosé, R, 2004. Nuclear waste disposal simulations: complex test cases. *Comput. Geosci.* 8 (2), 99–124.
- Hoteit, H, Firoozabadi, A, 2005. Multicomponent fluid flow by discontinuous Galerkin and mixed methods in unfractured and fractured media. *Water Resour. Res.* 41 (11), W11412.
- Hoteit, H, Firoozabadi, A, 2008. An efficient model for incompressible two-phase flow in fractured media. *Adv. Water Resour.* 31, 891–905.
- Huggenberger, P, Zidane, A, Zechner, E, Gechter, D, 2015. The role of tectonic structures and density-driven groundwater flow for salt karst formation. *Eng. Geol. Soc. Territ.* 5, 609–612 Volume.
- Hyman, JD, Karra, S, Makedonska, N, Gable, CW, Painter, SL, Viswanathan, HS, 2015. DFNWORKS: a discrete fracture network framework for modeling subsurface flow and transport. *Comput. Geosci.* 84, 10–19.
- Karimi-Fard, M, Durlafsky, LJ, Aziz, K, 2004. An efficient discrete-fracture model applicable for general purpose reservoir simulators. *SPE J.* 9, 227–236.
- Kim, JG, Deo, MD, 2000. Finite-element, discrete-fracture model for multiphase flow in porous media. *Alche J.* 46 (6), 1120–1130.
- Kozdon, J, Mallison, B, Gerritsen, M, Chen, W, 2011. Multidimensional upwinding for multiphase transport in porous media. *SPE J.* 16, 263–272 *SPE Reservoir Simulation Symposium*, The Woodlands, TX, Feb 02–04, 2009.
- Li, L., Lee, S.H., 2008. Efficient field-scale simulation of black oil in a naturally fractured reservoir through discrete fracture networks and homogenized media. *Soc. Petrol. Eng.* <https://doi.org/10.2118/103901-PA>.
- Makedonska, N, Painter, SL, Bui, QM, Gable, CW, Karra, S, 2015. Particle tracking approach for transport in three-dimensional discrete fracture networks. *J. Comput. Geosci.* <https://doi.org/10.1007/s10596-015-9525-4>.
- Martin, V, Jaffre, J, Roberts, J, 2005. Modeling fractures and barriers as interfaces for flow in porous media. *Siam J. Sci. Comput.* 26 (5), 1667–1691.
- Matthäi, SK, Mezentsev, A, Belayneh, M, 2007a. Finite element node-centered finite-volume experiments with fractured rock represented by unstructured hybrid element meshes. *SPE Reserv. Eval. Eng.* 10 (6), 740–756.
- Matthäi, SK, Geiger, S, Roberts, SG, Paluszny, A, Belayneh, M, Burri, A, Mezentsev, A, Lu, H, Coumou, D, Driesner, T, Heinrich, CA, 2007b. In: *Numerical Simulation of Multiphase Fluid Flow in Structurally Complex Reservoirs*, 292. Special Publications. Geological Society, London, pp. 405–429.
- Matringe, SF, Juanes, R, Tchepeli, HA, 2009. A new mixed finite element and its related finite volume discretization on general hexahedral grids. *Mech. Sol. Struct. Fluids* 12, 77–87.
- Moinfar, A, Varavei, A, Sepehrnoori, K, Johns, RT, 2014. Development of an efficient embedded discrete fracture model for 3D compositional reservoir simulation in fractured reservoirs. *Soc. Petrol. Eng.* <https://doi.org/10.2118/154246-PA>.
- Moortgat, J, Firoozabadi, A, 2016. Mixed-hybrid and vertex-discontinuous-Galerkin finite element modeling of multiphase compositional flow on 3D unstructured grids. *J. Comput. Phys.* 315, 476–500.
- Mosé, R, Siegel, P, Ackerer, P, Chavent, G, 1994. Application of the mixed hybrid finite element approximation in a ground water flow model: luxury or necessity? *Water Resour. Res.* 30 (11), 3001–3012.
- Nejati, M, Paluszny, A, Zimmerman, RW, 2015. On the use of quarter-point tetrahedral finite elements in linear elastic fracture mechanics. *Eng. Fract. Mech.* 144, 194–221.
- Nick, HM, Matthäi, SK, 2011. Comparison of three FE-FV numerical schemes for single- and two-phase flow simulation of fractured porous media. *Transp. Porous. Med.* 90, 421–444. <https://doi.org/10.1007/s11242-011-9793-y>.
- Noorishad, J, Mehran, M, 1982. An upstream finite element method for solution of transient transport equation in fractured porous media. *Water Resour. Res.* 18 (3), 588–596.
- Nordbotten, J, Aavatsmark, I, Eigestad, G, 2007. Monotonicity of control volume methods. *Nu Merische Mathematik* 106, 255–288.
- Peng, DY, Robinson, DB, 1976. A new two-constant equation of state. *Ind. Eng. Chem. Fundam.* 15, 59–64.

- Reiter, S, Logashenko, D, Grillo, A, Wittum, G, 2012. Preparation of grids for simulations of groundwater flow in fractured porous media. *Comput. Visual Sci.* <https://doi.org/10.1007/s00791-013-0210-7>.
- Reichenberger, V, Jakobs, H, Bastian, P, Helmig, R, 2006. A mixed-dimensional finite volume method for multiphase flow in fractured porous media. *Adv. Water Res.* 29, 1030–1036.
- Salama, A, Sun, S, El Amin, MF, 2013. A multipoint flux approximation of the steady-state heat conduction equation in anisotropic media. *J. Heat Transf.* 135 (4), 041302.
- Sandve, TH, Berre, I, Nordbotten, JM, 2012. An efficient multi-point flux approximation method for Discrete Fracture–Matrix simulations. *J. Comput. Phys.* 231, 3784–3800.
- Schmid, KS, Geiger, S, Sorbie, KS, 2013. Higher order FE–FV method on unstructured grids for transport and two-phase flow with variable viscosity in heterogeneous porous media. *J. Comput. Phys.* (241) P416–P444.
- Si, H. TetGen. A quality tetrahedral mesh generator and a 3D delaunay triangulator, <http://wias-berlin.de/software/tetgen/>, 2011.
- Siegel, P, Mosé, R, Ackerer, P, Jaffre, J, 1997. Solution of the advection-diffusion equation using a combination of discontinuous and mixed finite elements. *Int. J. Numer. Methods Fluids* 24 (6), 595–613.
- Tene, M, Bosma, S.B.M., Al Kobaisi, M.S., Hajibeygi, H., 2017. Projection-based embedded discrete fracture model (pEDFM). *Adv. Water Resour.* 105, 205–221.
- Unsal, E, Stephan, K, Matthäi, SK, Martin, JB, 2010. Simulation of multiphase flow in fractured reservoirs using a fracture-only model with transfer functions. *Comput. Geosci.* 14, 527–538. <https://doi.org/10.1007/s10596-009-9168-4>.
- Warren, J, Root, P, 1963. The behavior of naturally fractured reservoirs. *SPE J.* 3, 245–255.
- Watts, JW, 1986. A compositional formulation of the pressure and saturation equations. *SPE Reserv. Eng.* 1 (3), 243–252.
- Wheeler, MF, Yotov, I, 2006. A multipoint flux mixed finite element method. *SIAM J. Numer. Anal.* 44 (5), 2082–2106.
- Wheeler, M, Xue, G, Yotov, I, 2011. A family of multipoint flux mixed finite element methods for elliptic problems on general grids. *Procedia Comput. Sci.* (4) 918–927.
- Wheeler, M, Xue, G, Yotov, I, 2012. A multipoint flux mixed finite element method on distorted quadrilaterals and hexahedra. *Numerische Mathematik* (121) 165–204.
- Xing, F, Masson, R, Lopez, S, 2017. Parallel vertex approximate gradient discretization of hybrid dimensional Darcy flow and transport in discrete fracture networks. *Comput. Geosci.* 21, 595. <https://doi.org/10.1007/s10596-016-9606-z>.
- Younes, A, Konz, M, Fahs, M, Zidane, A, Huggenberger, P, 2011. Modelling variable density flow problems in heterogeneous porous media using the method of lines and advanced spatial discretization methods. *Math. Comput. Simul.* 81, 2346–2355.
- Younes, A, Makradi, A, Zidane, A, Shao, Q, Bouhala, L, 2014. A combination of Crouzeix–Raviart, Discontinuous Galerkin and MPFA methods for buoyancy-driven flows. *Int. J. Numer. Methods Heat Fluid Flow* 24 (3), 735–759.
- Younes, A, Fahs, M, Zidane, A, Huggenberger, P, Zechner, E, 2015. A new benchmark with high accurate solution for hot–cold fluids mixing. *Heat Mass Transf.* 51 (9), 1321–1336.
- Younes, A, Fahs, M, Belfort, B, 2013. Monotonicity of the cell-centred 644 triangular MPFA method for saturated and unsaturated flow in heterogeneous porous media. *J. Hydro.* 504, 132–141.
- Zidane, A, Younes, A, Huggenberger, P, Zechner, E, 2012. The Henry semi-analytical solution for saltwater intrusion with reduced dispersion. *Water Resour. Res.*
- Zidane, A, Zechner, E, Huggenberger, P, Younes, A, 2014a. On the effects of subsurface parameters on evaporite dissolution (Switzerland). *J. Contam. Hydrol.* 160, 42–52. <http://dx.doi.org/10.1016/j.jconhyd.2014.02.006>.
- Zidane, A, Zechner, E, Huggenberger, P, Younes, A, 2014b. Simulation of rock salt dissolution and its impact on land subsidence. *Hydrol. Earth Syst. Sci.* 18 (6), 2177–2189.
- Zidane, A, Firoozabadi, A, 2014. An efficient numerical model for multicomponent compressible flow in fractured porous media. *Adv. Water Resour.* 74, 127–147.
- Zidane, A, Firoozabadi, A, 2015. An implicit numerical model for multicomponent compressible two-phase flow in porous media. *Adv. Water Resour.* 85, 64–78.
- Zidane, A, Firoozabadi, A, 2017. Fracture cross-flow equilibrium in compositional two-phase reservoir simulation. *SPE J.* <https://doi.org/10.2118/184402>.